

Three-Flavor Gravitationally-Induced Neutrino Oscillations and the Solar Neutrino Problem

J. R. Mureika*
and

R. B. Mann†

*Department of Physics
University of Waterloo
Waterloo, Ontario N2L 3G1 Canada*

September 24, 2021

Abstract

Some implications of the proposal that flavor nondiagonal couplings of neutrinos to gravity might resolve the solar neutrino problem are considered in the context of three neutrino flavors. The two-flavor model is discussed as a limiting case of the full three-generation mechanism, and the behavior of the ν_e survival probability for various values of the three-flavor parameters is studied. Overlapping allowed SNU regions are obtained for the neutrinos which most likely contribute to the observed solar neutrino deficiency, and the effects of the addition of a third flavor are discussed. The extension to a three-generation framework is found to yield a greater allowed region

*newt@avatar.uwaterloo.ca

†mann@avatar.uwaterloo.ca

of parameter space, suggesting that gravitationally-induced neutrino oscillations remain a viable explanation of the Solar Neutrino Problem.

WATPHYS TH-96/02

1 Introduction

For three decades, resolution of the Solar Neutrino Problem (SNP) has eluded experimental and theoretical particle physicists alike. There are now four independent experiments for which the observed incident ν_e fluxes and events [1] have consistently been less than half the predicted rate, according to the various existing standard solar models [2].

A myriad of adjustments to existing astrophysical and particle models have been made in an attempt to resolve the SNP. These range from alterations of various solar models to changes in the fundamental properties of the neutrinos themselves, typically by modifying the physics of neutrinos so as to permit neutrino oscillations. The most popular of these latter proposals is the MSW (oscillation) Mechanism [3, 4], in which neutrinos (like quarks) are assumed to possess distinct non-trivial flavor *and* mass eigenbases in which their state evolution may be described. These are related by a unitary rotation matrix, and it is from this relation that the flavor-oscillation behavior arises in the equations of motion.

As there is at present no direct experimental evidence that neutrinos have mass it is worthwhile considering other possible mechanisms which could give rise to neutrino oscillations. One such possibility was proposed several years ago by Gasperini [6], who noted that if each flavor of neutrino ν_i possesses a different gravitational coupling G_i , then neutrino oscillations would be induced by gravitational effects. This mechanism violates the (Einstein) Equivalence Principle in the neutrino sector and has recently been dubbed the VEP mechanism [7]. However it admits neutrino oscillations for neutrinos of degenerate or zero mass, and so stands out as an interesting alternative to the mass oscillation mechanism¹.

To date, all analyses [6, 7, 8, 9, 10] of solar neutrino data utilizing the VEP model have been performed with only two flavors of neutrinos. There is some debate as to whether or not the allowed (two-dimensional) parameter space is large enough to validate a solution therein [9, 7]. More recently, it has been pointed out [10] that an improvement on the recent LSND experiments [11] have the potential for significantly constraining (or even ruling out) the VEP mechanism in conjunction with solar and atmospheric data.

¹Both mechanisms are not mutually exclusive. There have been several papers which have considered a massive-VEP oscillation mechanism, where the neutrinos possess *three* distinct eigenbases (electroweak, massive, and gravitational) [6, 12].

Motivated by the above, we consider in this paper a study of the realistic three-flavor VEP mechanism in the context of the SNP. We analyze current solar neutrino data to obtain the allowed regions of parameter space in the 3-generation VEP mechanism. To simplify the analysis, we shall assume that the mixing matrix transforming the gravitational eigenstates to weak ones is real (*i.e.* no CP-violating parameter in this sector). We show how the two-flavor “limit” may indeed be recovered for various values of mixing angles, and study the effects of hierarchy breaking in the violation parameters of the ν_μ and ν_τ . We compute the ν_e -survival probability surfaces for the three flavor case. We conclude with a discussion of the viability of the three flavor VEP mechanism as a solution to the SNP.

2 Three-Flavor VEP Oscillation Formalism

For N_g flavors of massless neutrinos, the Lagrangian may be written

$$\mathcal{L} = i \sum_{i=1}^{N_g} e(G_i) \bar{\nu}_{G_i} e^{a\mu}(G_i) \gamma_a D_\mu(G_i) \nu_{G_i} + \text{electroweak interactions} . \quad (1)$$

As usual, e_μ^a are the vierbeins, γ_a the Dirac matrices, and $e(G_i) \equiv \det\{e_\mu^a(G_i)\}$. Here, G_i are the flavor-dependent gravitational coupling constants, and we denote

$$G_i \equiv (1 + f_i)G , \quad (2)$$

where $f_i \ll 1$ are the VEP parameters which will play a role similar to that of the neutrino masses in the more conventional MSW mechanism. Here G is Newton’s constant as defined by the coupling of baryonic/photonic matter to gravity.

We define the neutrino eigenstates as

$$|\nu_W\rangle = \begin{pmatrix} \nu_e \\ \nu_\mu \\ \nu_\tau \end{pmatrix} , \quad |\nu_G\rangle = V_3 |\nu_G\rangle , \quad (3)$$

where $|\nu_W\rangle$ is the weak eigenbasis and $|\nu_G\rangle$ the gravitational eigenbasis. The matrix V_3 is the 3×3 leptonic analogue of the CKM mixing matrix, which can be parametrized as

$$V_3 = e^{i\theta_{23}\lambda_7} e^{-i\theta_{13}\lambda_5} e^{i\theta_{12}\lambda_2} , \quad (4)$$

where θ_{ij} are the vacuum mixing angles between flavors i and j , respectively. We have chosen V_3 to be real ($\delta = 0$), such that no CP violation occurs in the neutrino sector. This is done for simplicity, as there is nothing to rule out the possibility of such a violation. The λ_i are the SU(3) generators, whose representation is chosen such that V_3 takes on the form of the CKM (quark) mixing matrix.

Explicitly,

$$V_3 = \begin{pmatrix} c_{12}c_{13} & s_{12}c_{13} & s_{13} \\ -s_{12}c_{23} - c_{12}s_{13}s_{23} & c_{12}c_{23} - s_{12}s_{13}s_{23} & c_{13}s_{23} \\ s_{12}s_{23} - c_{12}s_{13}c_{23} & -c_{12}s_{23} - s_{12}s_{13}c_{23} & c_{13}c_{23} \end{pmatrix}, \quad (5)$$

where

$$c_{ij} = \cos \theta_{ij}, \quad s_{ij} = \sin \theta_{ij}. \quad (6)$$

For a spherically-symmetric curved spacetime with interior mass distribution $\mathcal{M}(r)$, we can write the linearized metric components [14]

$$\begin{aligned} g_{tt} &= 1 + \frac{2G\mathcal{M}(r)}{r} + o(G^2) \\ -g_{rr} &= 1 - \frac{2G\mathcal{M}(r)}{r} + o(G^2), \end{aligned} \quad (7)$$

in a heliocentric coordinate system. The neutrino path is chosen as purely radial.

Obtaining the appropriate vierbeins from (7), we use the massless Dirac equation to obtain a variant of the Weyl equation,

$$i \frac{d}{dr} |\nu_G\rangle = H |\nu_G\rangle, \quad (8)$$

with Hamiltonian

$$H \equiv -2E|\phi(r)|diag\{1 + f_i\} + H_{\text{weak}}, \quad (9)$$

where $\phi(r)$ is the Newtonian potential

$$\phi(r) = -G \int d^3r' \frac{\rho(r')}{|r - r'|}, \quad (10)$$

with $\rho(r)$ the solar density.

Under the change of basis in (3), the evolution equations become

$$\implies i \frac{d}{dr} |\nu_W\rangle = H' |\nu_W\rangle, H' = -2E |\phi(r)| V_3 \mathcal{F} V_3^{-1} + \mathcal{A}(r), \quad (11)$$

where H' is off-diagonal in the violation parameters and mixing angles, and

$$\begin{aligned} \mathcal{F} &= \begin{pmatrix} 0 & 0 & 0 \\ 0 & \Delta f_{21} & 0 \\ 0 & 0 & \Delta f_{31} \end{pmatrix} \\ \mathcal{A}(r) &= \begin{pmatrix} \sqrt{2} G_F N_e(r) & 0 & 0 \\ 0 & 0 & 0 \\ 0 & 0 & 0 \end{pmatrix}. \end{aligned} \quad (12)$$

Note that \mathcal{F} (or alternatively, H') is defined modulo a total factor of unity $\mathbb{1} \cdot f_1$, which merely results in an unobservable overall phase shift in the wavefunction. Here, $\mathcal{A}(r)$ is the energy shift in the ν_e sector, due to charged-current interactions in H_{weak} , $N_e(r)$ is the density of electrons and $\phi(r)$ is the radially-dependent solar potential.

It is convenient to find a new *matter-enhanced* basis $|\nu_M\rangle$ in which the Hamiltonian will once again be diagonal. We define

$$i \frac{d}{dr} |\nu_M\rangle = H'' |\nu_M\rangle, H'' = V_3^m H' (V_3^m)^{-1}, \quad (13)$$

The matter-enhanced mixing matrix V_3^m in (13) required to re-diagonalize the evolution equations is identical in form to (5), after the substitution:

$$\theta_{ij} \rightarrow \theta_{ij}^m, \quad (14)$$

with θ_{ij}^m the matter-enhanced mixing angles. These are somewhat more complicated in the three flavor case. For our purposes we shall only require the angles θ_{12} and θ_{13} :

$$\begin{aligned} s_{m12}^2 &= \frac{-(F_2^2 - \alpha F_2 + \beta) \Delta F_{31}}{\Delta F_{32} (F_1^2 - \alpha F_1 + \beta) - \Delta F_{31} (F_2^2 - \alpha F_2 + \beta)} \\ s_{m13}^2 &= \frac{F_3^2 - \alpha F_3 + \beta}{\Delta F_{31} \Delta F_{32}}, \end{aligned} \quad (15)$$

with

$$\begin{aligned}
F_1 &= f_1 + \frac{1}{3} \left\{ A - \sqrt{A^2 - 3BS} - \sqrt{3(A^2 - 3B)(1 - S^2)} \right\} \\
F_2 &= f_1 + \frac{1}{3} \left\{ A - \sqrt{A^2 - 3BS} + \sqrt{3(A^2 - 3B)(1 - S^2)} \right\} \\
F_3 &= f_1 + \frac{1}{3} \left\{ A + 2\sqrt{A^2 - 3BS} \right\} ,
\end{aligned} \tag{16}$$

and

$$\begin{aligned}
\alpha &= f_3 c_{13}^2 + f_2 (c_{12}^2 c_{13}^2 + s_{13}^2) + f_1 (s_{12}^2 c_{13}^2 + s_{13}^2) \\
\beta &= f_3 c_{13}^2 (f_2 c_{12}^2 + f_1 s_{12}^2) + f_2 f_1 s_{13}^2 \\
A &= \Delta f_{21} + \Delta f_{31} + D \\
B &= \Delta f_{21} \Delta f_{31} + D \left[\Delta f_{31} (c_{12}^2 c_{13}^2 + s_{13}^2) \right] \\
C &= D \Delta f_{21} \Delta f_{31} c_{12}^2 c_{13}^2 \\
S &= \cos \left\{ \frac{1}{3} \cos^{-1} \left(\frac{2A^3 - 9AB + 27C}{2(A^2 - 3B)^{3/2}} \right) \right\} \\
D &= \frac{\sqrt{2}}{2E|\phi(r)|} G_F N_e(r) .
\end{aligned} \tag{17}$$

The MSW analogues of these parameters can be found in [15, 16], and are related to the VEP terms in eqs. (17) via the substitution

$$\frac{\Delta m_{ij}^2}{2E} \rightarrow 2E|\phi(r)|\Delta f_{ij} . \tag{18}$$

The trademark difference between the two oscillation mechanisms is in their energy dependence: VEP effects are proportional to the neutrino energy E , while in the MSW case they are inversely proportional to E . That is, we have

$$\begin{aligned}
\langle P(\nu_e \rightarrow \nu_e) \rangle_{VEP} &\sim \mathcal{F}(E|\phi|\Delta f_{ij}) \\
\langle P(\nu_e \rightarrow \nu_e) \rangle_{MSW} &\sim \mathcal{F}\left(\frac{\Delta m_{ij}^2}{E}\right)
\end{aligned} \tag{19}$$

This is clear from the definition of D in (17). The authors of [9] suggest that an energy-resolution of less than 20% in the SNO and Superkamiokande detectors would be sufficient to discriminate between VEP and MSW suppression.

Solving (13) for $|\nu_e\rangle$, the full (averaged) three-flavor ν_e survival probability can be written as

$$\begin{aligned}
\langle P(\nu_e \rightarrow \nu_e) \rangle &= \sum_{i,j=1}^3 |(V_3)_{1i}|^2 |(P_{LZ})_{ij}|^2 |(V_3^m)_{1j}|^2 \\
&= c_{m12}^2 c_{m13}^2 \left\{ (1 - P_1) c_{12}^2 c_{13}^2 + P_1 s_{12}^2 c_{13}^2 \right\} \\
&\quad + s_{m12}^2 c_{m13}^2 \left\{ P_1 (1 - P_2) c_{12}^2 c_{13}^2 + (1 - P_1)(1 - P_2) s_{12}^2 c_{13}^2 + P_2 s_{13}^2 \right\} \\
&\quad + s_{m13}^2 \left\{ P_1 P_2 c_{12}^2 c_{13}^2 + P_2 (1 - P_1) s_{12}^2 s_{13}^2 + (1 - P_2) s_{13}^2 \right\} .
\end{aligned} \tag{20}$$

We may parameterize the non-zero probability of level crossing by a matrix P_{LZ} of the form [17]

$$\begin{aligned}
P_{LZ} &= \begin{pmatrix} 1 & 0 & 0 \\ 0 & \sqrt{1 - P_2} & \sqrt{P_2} \\ 0 & -\sqrt{P_2} & \sqrt{1 - P_2} \end{pmatrix} \begin{pmatrix} \sqrt{1 - P_1} & \sqrt{P_1} & 0 \\ -\sqrt{P_1} & \sqrt{1 - P_1} & 0 \\ 0 & 0 & 1 \end{pmatrix} \\
&= \begin{pmatrix} \sqrt{1 - P_1} & \sqrt{P_1} & 0 \\ -\sqrt{P_1(1 - P_2)} & \sqrt{(1 - P_1)(1 - P_2)} & \sqrt{P_2} \\ \sqrt{P_1 P_2} & -\sqrt{P_2(1 - P_2)} & \sqrt{1 - P_2} \end{pmatrix} \tag{21}
\end{aligned}$$

The terms P_1 and P_2 are the Landau-Zener jump probabilities for the $\nu_e \rightarrow \nu_\mu$ and $\nu_e \rightarrow \nu_\tau$ transitions, respectively, and are given by [7]

$$P_i = \frac{e^{-\eta_i} - e^{-\xi_i}}{1 - e^{-\xi_i}} , \tag{22}$$

where

$$\xi_i = 2\pi\kappa_i \left(\frac{\cos 2\theta_{1i}}{\sin^2 2\theta_{1i}} \right) , \quad \eta_i = \frac{\pi}{2}\kappa_i(1 - \tan^2 \theta_{1i}) . \tag{23}$$

The functions κ_i are the adiabaticity parameters for the $1i$ -transitions [7],

$$\kappa_i = \frac{\sqrt{2} G_F (N_e)_{res} \tan^2 2\theta_{1j}}{\left| \frac{1}{N_e} \frac{dN_e}{dr} - \frac{1}{\phi} \frac{d\phi}{dr} \right|} , \tag{24}$$

which are adiabatic for $\kappa_i \gg 1$, and highly non-adiabatic for $\kappa_i \leq 1$.

The definition of κ given in eq. 24 differs from its MSW analogue in the addition of the potential differential term $\frac{1}{\phi} \frac{d\phi}{dr}$. However, this addition does not account for a sizable variation in the value of the denominator. The ambient solar electron density $N_e(r)$ varies by several orders of magnitude in the interval $[0, R_\odot]$, which the potential $\phi(r)$ increases by a less than a factor of 10. Indeed, there is some debate as to whether VEP oscillations are dominated by the solar potential or by the larger (and constant) potential of the local supercluster [23].

We close this section by noting that the study of (20) can be greatly simplified by considering certain special cases of θ_{1i}^m , which are reflected in the interaction between the ν_e s and the surrounding matter. Since the ambient solar electron density $N_e(r)$ strictly decreases in the interval $r \in [0, R_\odot]$, then neutrinos can either be created above or below their resonance density. If the former holds, then the ν_e -creation density $(N_e)^{cr}$ is interior to the resonance density $(N_e)_{1i}^{res}$, and so the ν_e will pass through a resonance as it propagates outward. Conversely, if $(N_e)^{cr} < (N_e)_{1i}^{res}$, the ν_e will never undergo resonance, and will propagate as if in a vacuum². As a special case of this, we consider only $(N_e)^{res} > (N_e)_{max}$, *i.e.* the ν_e resonance density exceeds the maximal solar electron density.

The values of the matter-enhanced mixing angles θ_{ij}^m are determined by the resonance conditions. In the case $(N_e)^{cr} \leq (N_e)_{max} \ll (N_e)_{1i}^{res}$, generally $\Delta f_{i1} \gg D(r)$. Conversely, the D term in (17) will dominate in Eqs. (15) for $(N_e)^{cr} \gg (N_e)_{1i}^{res}$. Thus, it can be shown from Eqs. (16) and (17) that the matter mixing angles θ_{1i}^m will hence behave as follows in the two aforementioned scenarios:

$$(N_e)^{cr} \gg (N_e)_{12,13}^{res} : \quad \theta_{12}^m, \theta_{13}^m \rightarrow \frac{\pi}{2} \quad (25)$$

$$(N_e)_{12,13}^{res} > (N_e)_{max} : \quad \theta_{12}^m, \theta_{13}^m \rightarrow \theta_{12}, \theta_{13} . \quad (26)$$

We caution, however, that (26) holds *only if* there is a natural hierarchy in the VEP parameters, *i.e.* $\Delta f_{31} > \Delta f_{21}$. As we will later demonstrate, the

²For first generation neutrinos, we shall set $f_1 = 0$, and subsequently $f_j \neq 0, j \neq 1$. We make this choice based on the results of ref. [13], which we shall take to indicate that electron neutrinos (antineutrinos) and photons couple to gravity with strength G . Since the results we obtain are all dependent upon differences between the EEP-violating parameters f_i , this is not too restrictive an assumption.

behavior is quite different for a broken hierarchy (see Section 5). It should also be noted that the Landau–Zener jumps P_i vanish if the corresponding resonance density exceeds $(N_e)_{max}$.

3 The Two–Flavor Limit

Before proceeding to investigate the three-flavor model, we shall first examine the two–flavor limit.

We consider only the contributions of three types of solar neutrinos: 8B , 7Be , and pp. These contributions turn out to be the largest for all detectors currently in use. For example, we have calculated the unreduced counting rate contribution from the 8B and 7Be neutrinos to the ^{37}Cl detector to be $R_{sB} = 6.24$ SNU and $R_{7Be} = 1.13$ SNU using data from [18]. Combined, these rates account for 93.3% of the total SSM rate in Table 2. For the ^{71}Ga detectors, the equivalent unreduced rates are $R_{pp} = 70.94$ SNU, $R_{7Be} = 34.40$ SNU, and $R_{sB} = 14.53$ SNU, comprising 90.8% of the total predicted rate.

Two–generation oscillation analyses can be considered as special limiting cases of the full three–flavor model. Specifically, they result when the ν_τ (or ν_μ , for a broken hierarchy) totally decouples from the rest of the interactions, effectively reducing the 3×3 matrix V_3 to a 2×2 matrix R_2 plus a sterile neutrino.³

To do this, we must adhere to the following constraints, (i) : $(N_e)_{13}^{res} > (N_e)_{max}$, and (ii): $\theta_{13} = 0$. The former is satisfied for solar neutrinos of $E > 0.2$ MeV if $E\Delta f_{31} > 10^{-12}$ MeV, and so $\theta_{13}^m \rightarrow \theta_{13}$ and $P_2 \rightarrow 0$. Under these constraints, (20) successively reduces to

$$\langle P(\nu_e \rightarrow \nu_e) \rangle \tag{27}$$

$$(i) \rightarrow c_{m12}^2 c_{13}^2 \left\{ (1 - P_1) c_{12}^2 c_{13}^2 + P_1 s_{12}^2 c_{13}^2 \right\} \tag{28}$$

$$+ s_{m12}^2 c_{13}^2 \left\{ P_1 c_{12}^2 c_{13}^2 + (1 - P_1) s_{12}^2 c_{13}^2 \right\} + s_{13}^4$$

$$(ii) \rightarrow \frac{1}{2} + \left(\frac{1}{2} - P_1 \right) c_{2\theta_{12}^m} c_{2\theta_{12}} ,$$

³We note that the third neutrino need not be the ν_τ , as many theories incorporate a “fourth generation” neutrino, or supermassive neutrino, and so forth. Since we are considering a realistic three–generation analysis based on the Standard Model, though, we assume it to be the ν_τ .

which is Parke's formula [5]. For large ν_e creation densities ($(N_e)^c \gg (N_e)_{12}^{res}$), the preceding expression further simplifies to

$$\langle P(\nu_e \rightarrow \nu_e) \rangle = s_{12}^2 + P_1 c_{2\theta_{12}} . \quad (29)$$

A number of papers have been devoted to the study of gravitationally-induced neutrino oscillations in the two-flavor limit [6, 7, 8, 9, 12]. All of the results obtained are essentially commensurate with one another, despite the proposed controversy raised in [7], which assumed a disagreement in results between [8] and [9]. There was an apparent misunderstanding in ref. [7] of the conclusions in [9], which suggested that the SNU-curve overlap regions for two flavors of neutrinos were statistically too small to be viable. That is, according to [9] a χ^2 analysis associates a confidence level of less than 1% for the overlapping regions, for 2σ curves.

There are two main regions of overlap which have been found by all analyses done to date. These occur for small and large vacuum mixing angles, respectively. Figure 2 from [7] and Figure 2 from [9] can be referenced for comparison. Ref. [7] claims the overlap regions to be:

- Nonadiabatic: $\sin^2 2\theta \in [2 \times 10^{-3}, 10^{-2}]$, $\Delta f \in [2.7 \times 10^{-14}, 3.3 \times 10^{-14}]$
- Adiabatic: $\sin^2 2\theta \in [0.6, 0.9]$, $\Delta f \in [1.0 \times 10^{-16}, 1.5 \times 10^{-15}]$.

For comparison, [19] gives the approximate values of the overlap regions for the two-flavor MSW mechanism as: (1) nonadiabatic: ($\sin^2 2\theta \approx 7 \times 10^{-3}$, $\Delta m^2 \approx 1.75 \times 10^{-3} eV^2$), and (2) adiabatic: ($\sin^2 2\theta \approx 0.6$, $\Delta m^2 \approx 9 \times 10^{-6} eV^2$). These masses are roughly equivalent to the above values of Δf for neutrinos of energy ~ 10 MeV, where we have again assumed an *average* gravitational potential $|\phi| \sim 5 \times 10^{-6}$ for the Sun.

For large θ_{12} (*i.e.* $\sin^2 2\theta_{12} > 0.1$), the 12-jump term vanishes, *i.e.* $P_1 \rightarrow 0$, and $\langle P(\nu_e \rightarrow \nu_e) \rangle$ goes as s_{12}^2 , while for small θ_{12} , it is dominated by P_1 . From this, we see that the large θ_{12} solutions (adiabatic approximation) are energy independent, while the small θ_{12} ones (non-adiabatic) are very much dependent on the matter effects.

In the adiabatic region, the suppression is energy independent, and the fluxes of all types of solar neutrinos are equally reduced. This can be seen from (29) since the Landau-Zener term $P_{LZ} \rightarrow 0$ for adiabatic transitions, and we are left with $\langle P(\nu_e \rightarrow \nu_e) \rangle = \sin^2 \theta$. Meanwhile, the nonadiabatic

mixing region can be found for small vacuum mixing angles $\theta_{12} \sim 10^{-3}$. For small θ_{12} , the survival probability goes as P_{LZ} , which is generally large, except near resonance, where it can rapidly suppress almost the entire flux.

Using (29), the following results have been obtained. First, the ν_e suppression probabilities of [7] are accurately reproduced. The 2-flavor limit was taken by setting (i) $(N_e)_{13}^{res} \gg (N_e)_{max}$ ($\Delta f_{31} = 10^{-9}$, in this case), and (ii) $\theta_{13} = 0$. For all SNU-plots included in this work, we define the confidence level (CL) as the departure from the averaged value of the counting rates, as given in Table 1. Hence, a confidence level of 95% would include all calculated VEP-reduced rates which fall in the range of $rate \pm 2\sigma$, where σ is the quoted experimental error (see Table 1).

Counting rates for neutrinos from source α (e.g. ${}^8B, {}^7Be, pp$, etc...) are obtained via numerical integration of the equation

$$R_x^\alpha = \int_0^{R_\odot} dr r^2 \xi^\alpha(r) \int_{E_{min}}^{E_{max}} dE \phi^\alpha(E) \sigma_x(E) \langle P(\nu_e \rightarrow \nu_e) \rangle(r, E), \quad (30)$$

for neutrinos with energy spectrum $\phi^\alpha(E)$ and maximum energy E_{max} , incident on detector material x with absorption cross-section $\sigma_x(E)$. The function $\xi^\alpha(r)$ represents the fraction of neutrinos of type α produced at radius r .

With cross-sections $\sigma_x(E)$ and neutrino spectra $\phi^\alpha(E)$ from [2], we have calculated 2 and 3 σ overlap regions for a two-flavor limit. These are shown in Figs. 1, 2. Figure 1 clearly shows evidence for structure in the regions of the small and large mixing solutions, differing from the small tail connecting the two (diagonal line overlap).

In Fig. 2, the two overlap regions discussed previously can be seen amidst the lower statistically-viable areas (e.g. diagonal strip). A “new” region has opened up just above the location of the small mixing region, but this may simply be a manifestation of the overestimation mentioned earlier. Since only experimental errors are taken into account for this method, this explains the discrepancy between these plots and the iso-SNU curves of [7].

The errors in the theoretical fluxes are quite possibly a major source of the structural difference in the overlap region. We have generated plots for both the upper and lower flux limits for the neutrino sources considered (${}^8B, {}^7Be$, and pp). The 8B flux has an associated error of up to 37%, so we

should expect this to greatly determine the allowed regions. For discussion purposes, we will use as comparison only the 3σ level of overlap.

For the lower flux limit case (Fig. 3), the connecting arm is greatly expanded, implying that the shift in flux lowers the contours of one of the experiments more so than the others. These are most likely the ^{37}Cl contours, since the ^8B neutrinos are the primary candidates detected. The large mixing region tends to drop below the range indicated by previous studies (see *e.g.* [7, 21, 16],...) though, so we can assume that there is a lower weighting associated to this region of the flux errors. The structure of the upper flux limit (Fig. 4) is more like Fig. 2 than is Fig. 3. The new region has joined with the area of the small mixing solutions, while the large mixing region has “fattened”. Due to the similarities of Figs. 2 and 4, we can deduce that the statistically-average flux contribution to the counting rates tends to favor the higher end of the flux range, rather than the lower. A full χ^2 analysis of the data should reproduce the results cited earlier.

4 $\langle P(\nu_e \rightarrow \nu_e) \rangle$ Expressions for Specific Resonance Behavior with Three Flavors

Several researchers studying the three-flavor MSW oscillation mechanism ([3, 16, 21]) have concluded that interesting results can be obtained if the ν_e s undergo both $\nu_e \rightarrow \nu_\mu$, $\nu_e \rightarrow \nu_\tau$ resonances, *i.e.* $(N_e)^{cr} \gg (N_e)_{12,13}^{res}$. Accordingly, $\theta_{12,13}^m \rightarrow \frac{\pi}{2}$. Defining $s_{1i} = \sin \theta_{1i}$, $c_{1i} = \cos \theta_{1i}$, and similarly for s_{m1i}, c_{m1i} . the survival probability assumes the simpler form

$$\langle P(\nu_e \rightarrow \nu_e) \rangle = P_1 P_2 c_{12}^2 c_{13}^2 + P_2 (1 - P_1) s_{12}^2 s_{13}^2 + (1 - P_2) s_{13}^2, \quad (31)$$

since all c_{m1i} vanish.

The matter effects are not gone, due to the presence of the Landau-Zener jump terms. Like the two-flavor case, we examine the small and large angle effects on (31), except now we have four cases instead of two. The former are generally characterized by an overall P_i dependence, while the latter show energy independence ($P_i \rightarrow 0$).

4.1 Dependence on θ_{12}

First, let us consider the small and large θ_{12} cases, to show how the two-flavor cases change in the full three generation scenario.

Small θ_{12} :

$$\langle P(\nu_e \rightarrow \nu_e) \rangle = s_{13}^2 - P_2 \left\{ s_{13}^2(1 + P_1) - P_1 \right\} \quad (32)$$

Large θ_{12} :

$$\langle P(\nu_e \rightarrow \nu_e) \rangle = s_{13}^2(1 - P_2 c_{12}^2) \quad (33)$$

We immediately note a significant departure from the behavior of the two-flavor mechanism. In both cases, an explicit s_{13}^2 term will dominate for an appropriate choice of parameters, and the matter effects from the 13-resonance (via P_2) are always present. This dependence can have significant impact on the overall flavor conversion of solar ν_e s. Furthermore, we note that for small θ_{13} , equation (32) $\rightarrow P_1 P_2$ shows strong non-adiabatic dependence for both resonances, which can significantly change the shape of the suppression curve (see Figs.5,6). Meanwhile, (33) $\rightarrow 0$ as s_{13}^2 becomes small! Clearly, this implies an almost complete attenuation of ν_e s. This radically different behavior is indicative of the need to further study the effects of a third flavor. Note that both of these results are *not* approximations of the two-flavor mechanism, since the condition $\theta_{13}^m \rightarrow \frac{\pi}{2}$ is in place. A recovery of pure $\nu_e \rightarrow \nu_\mu$ oscillations requires the absence of the 13-resonance, i.e. $\theta_{13}^m \rightarrow \theta_{13} \rightarrow 0$.

4.2 Dependence on θ_{13}

A more relevant discussion of a full three-generation model hinges on the study of the dependence on the third flavor. In the previous subsection, we caught a glimpse of these effects in the small and large mixing regions.

Small θ_{13} :

$$\langle P(\nu_e \rightarrow \nu_e) \rangle = c_{12}^2 P_1 P_2 \quad (34)$$

Large θ_{13} :

$$\langle P(\nu_e \rightarrow \nu_e) \rangle = s_{13}^2 \quad (35)$$

It can easily be shown that (34) takes on both characteristics of the previous subsection for small and large θ_{12} . However, perhaps the most important

conclusion to be drawn from the analysis of flavor conversion in both 12– and 13–resonances is (35). In the three–flavor VEP (and MSW) mechanisms, the presence of a large θ_{13} completely dominates the ν_e suppression. This is visible in Figs. 7,8.

The significance of this is obvious: it is possible to choose the fraction of surviving solar ν_e s by fixing s_{13}^2 to the appropriate value. It is important to note that this is *independent of θ_{12}* , and hence independent of the 12–resonance.

We have verified the assertion in [19] that the very large θ_{13} solutions can be ruled out by present data. Figure 9 is clearly indicative that allowed regions can only exist for a very small range of parameters on the wall near resonance. The double–resonance and vacuum oscillations are intuitively ruled out, as in each case, $\langle P(\nu_e \rightarrow \nu_e) \rangle$ is either too large or too small, respectively.

4.3 No 12– or 13–resonances: Vacuum Oscillations

For values of $\Delta f_{21}, \Delta f_{31}$ which exceed $\sim 10^{-12}$, the ν_e s will not interact with matter. If this situation occurs, then the matter–enhanced mixing angles $\theta_{12}^m, \theta_{13}^m$ will take on their corresponding vacuum counterpart values, *i.e.* $\theta_{12}^m \rightarrow \theta_{12}, \theta_{13}^m \rightarrow \theta_{13}$. The probability then reverts to the trivial form

$$\langle P(\nu_e \rightarrow \nu_e) \rangle = c_{12}^4 c_{13}^4 + s_{12}^4 c_{13}^4 + s_{13}^4, \quad (36)$$

which is recognizable as (20), with $V_3^m = V_3$, and $P_{LZ} = \mathbb{1}$. There are several vacuum oscillation solutions which are still viable (see [19] for a brief discussion), although they are not considered in this analysis.

5 Broken Hierarchy: $\Delta f_{21} > \Delta f_{31}$

So far, we have examined the behavior of $\langle P(\nu_e \rightarrow \nu_e) \rangle$ for the two–flavor limit, as well as for the case of both resonances, assuming a natural hierarchy in the violation parameters. However (apart from mathematical and/or aesthetic prejudices) there is no *a-priori* reason to expect there to be such a hierarchy. In this section we consider the possibility that $\Delta f_{21} > \Delta f_{31}$, which we refer to as the broken-hierarchy case.

In effect, such a break in the natural scheme of things amounts to a reversal of the matter–enhanced energy–eigenvalues, and hence an interchange of vacuum and matter violation parameters $(f_2, f_3) \rightarrow (F_3, F_2)$ of Eqs. (16,17). To show this, we take the limiting form of these parameters when $f_2 \gg f_3$.

5.1 Case 1: No 12–resonance

For this condition to be satisfied, $E\Delta f_{21}$ must be set above the previously mentioned value. We assume that $(N_e)^{cr} \gg (N_e)_{31}^{res}$, in order that 13–resonances still take place. The matter–enhanced parameters become dominated by f_2 , and for convenience we may replace $f_2 \rightarrow \Delta f_{21}$ (since we define $f_1 \equiv 0$). This gives

$$\alpha \sim \Delta f_{21}(c_{13}^2 c_{12}^2 + s_{13}^2) \quad (37)$$

$$A \sim \Delta f_{21} \quad (38)$$

Also, from the definitions of F_i in eq. (16) we can show that

$$F_3 \sim \Delta f_{21}, \quad F_3 \gg F_2, F_1 \quad (39)$$

This implies that

$$F_3 \sim \Delta F_{31} \sim \Delta F_{32}, \quad (40)$$

and the additional parameters $\beta, C \rightarrow 0$, while $S \sim 1$. Therefore, we see that

$$\begin{aligned} s_{m13}^2 &= \frac{F_3^2 - \alpha F_3 + \beta}{\Delta F_{31} \Delta F_{32}} \quad (41) \\ &\sim \frac{F_3(F_3 - \alpha)}{F_3^2} \\ &= \frac{(\Delta f_{21})^2(1 - c_{12}^2 c_{13}^2 - s_{13}^2)}{(\Delta f_{21})^2} \end{aligned}$$

or

$$s_{m13}^2 = s_{12}^2 c_{13}^2. \quad (42)$$

Thus, instead of the naive replacement $s_{m13}^2 \rightarrow s_{12}^2$ that one might expect (since we are changing the roles of the eigenvalues), there is a non–trivial dependence on *both* vacuum mixing angles. If the 13–resonance still takes place, it can similarly be shown that the condition $s_{m12}^2 \sim 1$ still holds, *i.e.* $\theta_{12}^m \rightarrow \frac{\pi}{2}$.

5.2 Case 2: No 12– or 13–resonance

Neither resonance will take place if $(N_e)_{12,13}^{res} > (N_e)_{max}$, thus the solar ν_e s will propagate essentially as in vacuum. However, due to the “role–reversal” of the eigenvalues, the form of the oscillations will not be the same as (36). We have already seen that the behavior of s_{m12}^2 is different than that expected for $(N_e)_{12}^{res} > (N_e)_{max}$. In a similar fashion, we will obtain the broken hierarchy expression for s_{m13}^2 .

Recall that the matter–enhanced 12–oscillation term is

$$s_{m12}^2 = \frac{-(F_2^2 - \alpha F_2 + \beta)\Delta F_{31}}{\Delta F_{32}(F_1^2 - \alpha F_1 + \beta) - \Delta F_{31}(F_2^2 - \alpha F_2 + \beta)} \quad (43)$$

For the scenario in question, the eigenvalues F_2 and F_3 are dominated by f_3 and f_2 , respectively. Accordingly, the numerator of (43) will reduce to

$$\begin{aligned} & (F_2^2 - \alpha F_2 + \beta)\Delta F_{31} \\ \rightarrow & f_2 f_3^2 - f_2 f_3 [f_3 c_{13}^2 + f_2 (c_{12}^2 c_{13}^2 + s_{13}^2)] + f_2^2 f_3 c_{12}^2 c_{13}^2 \\ = & f_2 f_3^2 s_{13}^2 - f_2^2 f_3 s_{13}^2 \\ = & -(f_2^2 f_3 - f_2 f_3^2) s_{13}^2, \end{aligned} \quad (44)$$

while the denominator behaves as

$$\begin{aligned} & \Delta F_{32}(F_1^2 - \alpha F_1 + \beta) - \Delta F_{31}(F_2^2 - \alpha F_2 + \beta) \\ \rightarrow & (f_2 - f_3)\beta - f_2(f_3^2 - \alpha f_3 + \beta) \\ = & f_2^2 f_3 c_{12}^2 c_{13}^2 - f_2 f_3^2 c_{12}^2 c_{13}^2 - f_2 f_3^2 s_{13}^2 + f_2^2 f_3 s_{13}^2 \\ = & (f_2^2 f_3 - f_2 f_3^2)(c_{12}^2 c_{13}^2 + s_{13}^2). \end{aligned} \quad (45)$$

The value of F_1 is typically several orders of magnitude smaller than the other F_i , thus we take $F_1/F_i \rightarrow 0$ in the analysis (note that $F_1 \rightarrow 0$ for full flavor–resonance). Since we set $f_1 = 0$, the values of f_2, f_3 and $\Delta f_{21}, \Delta f_{31}$ are respectively identical. Thus, (43) reduces to a simple expression. For vacuum oscillations in a broken hierarchy scheme, the matter–enhanced mixing angles assume the modified forms

$$s_{m12}^2 = \frac{s_{13}^2}{s_{13}^2 + c_{12}^2 c_{13}^2} \quad (46)$$

$$s_{m13}^2 = s_{12}^2 c_{13}^2. \quad (47)$$

In general, the resulting suppression will be smaller for a broken hierarchy than for a natural one (as shown in Figs. 7, 8). For small θ_{13} , we see that (46) approaches 0, while (47) approaches s_{12}^2 . This is consistent with the decoupling of the third neutrino, except here the decoupled flavor is the ν_μ . If both θ_{12} and θ_{13} are small, the natural and broken hierarchical values of $\langle P(\nu_e \rightarrow \nu_e) \rangle$ are almost identical. For example, in the case of Fig. 5, the difference has been calculated as less than 0.001% for various violation parameter values (with $\Delta f_{21} > \Delta f_{31}$).

This implies that a broken hierarchy in the vacuum oscillation range would be almost indistinguishable from the natural case.

For larger angles, the fact that the flux reduction is greater than for the natural case can possibly be used to our advantage: a specific choice of mixing angles can lead to $\langle P(\nu_e \rightarrow \nu_e) \rangle$ which is too large to account for the observed fluxes. Conversely, the broken hierarchy vacuum oscillation $\langle P(\nu_e \rightarrow \nu_e) \rangle$ is smaller, and can conceivably fit the data in situations when the former cannot.

6 8B , 7Be , and pp Suppression

In the two-flavor case, we saw that the suppression pits for neutrinos of varying energies differed in size from each other (see [7]). In the following section, we will briefly examine these variations in the three-flavor model. For simplicity, we compare the 8B , 7Be , and pp neutrinos only in the large θ_{12} case. The curves for small θ_{12} show similar behavior. Note that all axes of the form $2E\Delta f_{i1}$ will be expressed in units of 10^{18} MeV^{-1} .

In Fig. 10, we see how the suppression radically varies over several orders of magnitude in $2E\Delta f_{31}$. We first consider the case of small θ_{13} , to show how the two-flavor results are affected by the addition of the ν_τ resonance. For relatively small values, we see the behavior indicated in Section 4.2, namely that small values of θ_{13} can lead to almost complete attenuation of the flux. The width of the suppression pit is almost the same as for the two-flavor scenario, which is approximated by the upper set of curves ($2E\Delta f_{31} = 2 \times 10^{-6}$).

However, several differences to note include the following: while each type of neutrino is equally suppressed along the upper pit-bottom, there is a greater amount of suppression for the pp and 7Be neutrinos in the lower

curve.

In fact, for the lower curve, the suppressions are too great to match the experimental values cited by the solar neutrino experiments. Also, for a broken hierarchy with one resonant flavor (visible in the lower curve of Fig. 10 for $2E\Delta f_{21} > 10^7$), we note that the pp neutrinos are suppressed *less* than the ${}^7\text{Bes}$ and ${}^8\text{Bs}$.

This should be contrasted with the regular two-flavor case, where in general the pp pits always end before those of the ${}^8\text{Bs}$. The kink behaviors visible in the upper curve of Fig. 10 are a result of crossing the hierarchy-boundary (i.e. the surface $2E\Delta f_{21} = 2E\Delta f_{31}$).

In contrast, Fig. 11 shows the same curves for large θ_{13} . The dominance of s_{13}^2 is clearly visible for the curve $2E\Delta f_{31} = 2 \times 10^4$.

Also visible is the inversion of energy suppression for the case of the broken hierarchy. In the case of only $\nu_e \rightarrow \nu_\tau$ resonance, the pp neutrinos are suppressed less than the ${}^8\text{B}$ neutrinos. The full effect of the third flavor is visible in the $2E\Delta f_{31} = 2 \times 10^6$ curve. This represents the ν_τ above resonance, but with large mixing angle θ_{13} , and should be compared with the two-flavor case from [7]. The variation in suppression of differing energies is also very striking: the pp neutrinos are suppressed much more than are the ${}^8\text{Bs}$ in this case, such that the flat pit bottoms do not even overlap. The average energies of the ${}^7\text{Be}$ and pp neutrinos are an order of magnitude less than those of the ${}^8\text{Bs}$. Hence, when the ${}^8\text{B}$ neutrinos have energies $2E\Delta f_{31} > 10^{-12}$, the pp and ${}^7\text{Be}$ will not. Thus, there can be a double resonance behavior for certain types of neutrinos, while others have only one.

This yields interesting possibilities if experiment dictates the various fluxes are suppressed by different amounts. However, since it is generally the case that the ${}^8\text{B}$ flux is attenuated to a higher degree than is the pp flux, this behavior probably cannot account for the flux deficit. The broken hierarchy single-resonance cases discussed earlier can provide viable solutions if data requires varying degrees of reduction for each flux, since the ${}^8\text{B}$ are more suppressed than the pp neutrinos are.

In the regular two-flavor case, overlap regions requiring differently suppressed fluxes can only occur on the pit walls, implying only a small allowed area of parameter space. Adjacent flat-bottom $\langle P(\nu_e \rightarrow \nu_e) \rangle$ curves of differing values can provide a much larger acceptable parameter space region to match experiment.

For the case of extremely large θ_{13} mentioned in Section 4.2, Fig. 12 shows curves for $2E\Delta f_{31} = 2 \times 10^4$ and 2×10^6 . For both sets of curves, the neutrinos of lower energies are always suppressed to a greater extent than those of higher energies (except for the $2E\Delta f_{31}$ curve, which goes as $s_{13}^2 = 0.8$, as with large θ_{13} behavior, before the resonance boundary). For the leftmost curves, the pp flux can be attenuated by almost a factor of 2 more than the 8B neutrinos in places along the pit wall, with the 7Be suppression somewhere in between. Depending on the input values of the fluxes, this can perhaps provide a viable solution. The $2E\Delta f_{31} = 2 \times 10^6$ curve shows much more constraining behavior, though, with an extremely steep pit wall (partially due to hierarchical inversion) over a short range of $2E\Delta f_{21}$ values, much akin to the pit wall of the non-adiabatic 2-flavor solution. It seems rather unlikely that a statistically significant overlap region of parameter space can open for these energies, since the method of calculation used in this paper tends to overestimate the allowed regions.

7 Parameter Space Analysis for Three-Flavor Oscillations

In Section 6, we showed how the addition of a third flavor affects the suppression of ν_e fluxes for varying sources of neutrinos. Different types of neutrino fluxes (8B , 7Be , pp) are suppressed to differing degrees, depending on specific conditions such as double-resonance and single-resonance behavior, vacuum oscillations, broken hierarchies, and so forth. In this section we consider how all of these effects come together by studying the parameter space overlap regions for the experimental values cited in Table 1.

We shall focus on the regions of overlap as calculated by eq. (30). We present plots for 2 and 3σ C.L.s, as defined in Section 3, for the limiting conditions discussed in Section 4 *i.e.* large and small θ_{12} and θ_{13} values. We find that, particularly for the large θ_{13} solution, large areas of parameter space become viable overlap regions at the 3σ level.

As previously mentioned, one of the nicest ways to visualize the effect of the various oscillation models on solar neutrino rates is to look at the regions of parameter space which allow such solutions. In Section 3, we saw the limiting case of two flavors, and how this compared with other two-generation

studies. Again, before reviewing the following results, it should be stressed that the allowed regions of parameter space discovered in this Section have been done so by straight numerical overlap, and hence can overestimate certain regions (again, see [20] for a detailed discussion on the different techniques for error treatment). Since the parameter space in question is actually four dimensional $(\theta_{12}, \theta_{13}, \Delta f_{21}, \Delta f_{31})$, we present the regions as “slices” of fixed $(\theta_{13}, \Delta f_{31})$. This is a natural choice, as it facilitates comparison with the allowed two-flavor SNU overlaps. We overlay the results with the two-generation allowed boundaries (see the referenced figures in [7, 9]), to show how the new degrees of freedom can introduced regions outside of these areas.

7.1 Small θ_{13}

So long as $(N_e)_{13}^{res} > (N_e)_{max}$, sufficiently small values of θ_{13} will recover the two-flavor model. However, as noted in Section 4, if $\Delta f_{31} < 10^{-12}$, then $s_{m13}^2 \rightarrow 1$, and $\langle P(\nu_e \rightarrow \nu_e) \rangle$ will take on a different form than for a single resonance. Unfortunately, (33) shows that the neutrino fluxes can almost be extinguished for the double-resonance region, where both $\Delta f_{21}, \Delta f_{31} < 10^{-12}$. If this is the case, then an overlap in parameter space for these values would most likely only appear at the 3σ C.L., as defined in this work.

Figure 13 attests to the low survival rate, showing only overlap regions for a broken hierarchy in the small θ_{12} range. This region is mostly due to the nonadiabatic contributions from the Landau-Zener Jump terms (see eq. (34)). At the 2σ C.L., the overlap regions completely vanish, so the plots are not included. Looking at the upper-flux limits for each neutrino source, though, we see a slightly different picture. Figure 14 shows the 3σ overlap regions for the same choice of parameters employed in Fig. 13, using only the upper bounds for each experimentally-observed rate. We see that a much larger region has opened up for this choice of fluxes, which implies that a small θ_{13} solution is very sensitive to the value of the flux. The lower flux range plot is very similar to Fig. 13. As the third flavor begins to decouple, *i.e.* $\Delta f_{31} \sim 10^{-12}$, the overlap regions for $s_{13}^2 = 10^{-3}$ vanish all together.

However, as we move down an order of magnitude, regions begin to open up once more. Figs. 15 and 16 show these regions for $s_{13}^2 = 10^{-4}$. Note that the region in Fig. 16 begins to take the form of the two-flavor region from Fig. 2.

7.2 Large θ_{13}

We begin to see new regions open up for values of θ_{13} which were not allowed for double-resonance. For example, large s_{13}^2 solutions begin to become more abundant. Figs. 17, 18, 19 show how the regions evolve with increasing 13-mixing angle. It should be noted that such behavior is *not* apparent for the previously discussed case of $\Delta f_{31} = 10^{-13}$. The only viable region in that case is $s_{13}^2 = 0.4$. Lower values of s_{13}^2 show previously unallowed vacuum oscillation regions for a broken hierarchy, much like Fig. 13.

This is due to the strong dependence on s_{13}^2 from the probabilities of Section 35. In fact, for a double-resonance (where the survival probability goes as $\langle P(\nu_e \rightarrow \nu_e) \rangle = s_{13}^2$) we should expect to see most of parameter space become viable. Indeed, Fig. 20 shows exactly this situation. The two-flavor boundaries are clearly ignored in this case, as the 13-resonance dominates the suppression. The problem with such a solution is that despite the excellent mobility it gives one in parameter space, the constraint imposed by the limiting form of $\langle P(\nu_e \rightarrow \nu_e) \rangle$ severely impedes much leeway from set counting rates.

Fig. 21 testifies to this fact. Essentially, this is a result of the counting rates being “fixed” to a value of $R_{VEP} \sim R_{SSM} \times s_{13}^2$. If R_{VEP} is in the range $R_{expt} \pm 3\sigma_{expt}$, but not in the range $R_{expt} \pm 2\sigma_{expt}$, then Figs. 20 and 21 will be the result for the overlap regions.

If we examine the 3σ upper-flux limit of the large mixing region, then we see even more interesting behavior. Fig. 22 shows large bands which do not constitute viable regions of parameter space, with a central accepted area, and the regions below the 2-flavor adiabaticity boundary disappear. The sensitivity of the allowed overlaps becomes very apparent for large s_{13}^2 in this case.

7.3 SNU-Region Comparison: VEP v.s. MSW

We have seen how the SNU regions are commensurate with those calculated for the two-flavor VEP mechanism (see Section 3), and have also discussed the commonalities between two-flavor VEP and MSW regions. Here we compare the full three-generation VEP mechanism to previous findings from three-flavor MSW studies. However most studies of the MSW three-flavour case concentrate on a combined analysis of data from all types of neutrino

experiments. We shall reference the plots in [21], as these are exclusively fits of solar neutrino counting rates.

Ref. [21] presents the MSW overlap regions for the two-flavor limit, as well as small and large θ_{13} solutions, at the 1, 2, and 3σ C.L.s. Although the definition of the confidence level differs from that used here, it is still possible to compare the works based simply on the behavior of the regions for the different σ limits. In particular, [21] shows that the two-flavor limit overlap zones occur exclusively on the diagonal and vertical regions of the plots. This is due to the wide variation of ν_e survival probability behavior for the small and large 12-parameters (Δf_{21} or Δm_{21}^2 and θ_{12}). The horizontal solution is ruled out in this analysis as it implies a suppression of mostly high energy neutrinos, which contradicts the observed KII data (sensitive *only* to high energy neutrinos). The vertical solution represents energy-independent suppression (large-angle $\langle P(\nu_e \rightarrow \nu_e) \rangle$ behavior, see Section 3).

Meanwhile, for non-zero θ_{13} , the results are also very similar. The 1σ overlap regions are thin, and for the most part, do not exist on the horizontal or vertical portions of the SNU curves. As the analysis proceeds to the 3σ level, we see regions expanding and new ones opening up all over the parameter space in question. The work in [21] shows extremely large allowed regions for large θ_{13} at the 3σ level, which is similar to the results of Figs. 19, 20.

8 Discussion

We have examined the viability of extending the VEP oscillation mechanism from two neutrino flavors to the realistic three-generation model as a possible resolution to the SNP. We have studied the behavior of the ν_e survival probability $\langle P(\nu_e \rightarrow \nu_e) \rangle$ in various limiting cases, including a recovery of the two-flavor mechanisms. The concept of a broken hierarchy was compared to the natural one, to see how the dynamics could be used to one's advantage as a successful resolution of the SNP. A resulting examination of the SNU overlap regions in parameter space for the four cited experiments ensued.

So what conclusions can be drawn for the three-flavor VEP model? Does it expand or create new regions in parameter space? Certainly, the probability analysis of section 4 tends to point in favor of expansion; the dominance of large θ_{13} can yield enormous viable regions of parameter space. This was

demonstrated in the SNU plots of Section 7.3. However, due to the rigid constraints on the ν_e -suppression (see section 7.2), these regions hold only for large enough θ_{13} , and so generally disappear for lower confidence levels. A broken hierarchy opens the possibility of small θ_{12} oscillations, particularly if these occur in a single-resonance zone for $\nu_e \rightarrow \nu_\tau$ transitions only.

When compared to the overlap regions calculated in [21], we find that the results obtained in this paper are similar to those for an MSW analysis. In the limiting two-flavor case, they find that the only allowed regions are on the diagonal and vertical parts of the SNU curves, which is consistent with the figures of Section 3. This is due to the varied suppression in the fluxes (as discussed in Section 4). The diagonal is highly dependent on the nonadiabatic jump P_1 , while the vertical is representative of equal (energy independent) suppression for all fluxes (*i.e.* $\sim s_{12}^2$). At the quoted 3σ experimental levels of Table 1, these are both allowed.

For both two and three generation models, low confidence level overlap regions do not exist for either the horizontal or vertical areas (*i.e.* only on the vertical, or non-adiabatic, region). For higher C.L.s, they show extremely large and varied regions of overlap opening up. Up to method of calculation, these results are commensurate with the SNU plots presented in Sections 3 and 7. In particular, the 3σ large θ_{13} SNU plots of [21] are very similar in structure to those of Section 7. We have verified the assertion in [19] that a very large value of s_{13}^2 is effectively ruled out by the solar neutrino data. Since the work in [19] is based largely on a combined analysis of solar neutrino, oscillation (LSND), and reactor (Bugey) experiment data, no further comparisons can be made at this time.

We point out that, while VEP and MSW yield similar SNU plots, the differing energy dependence in eq. (19) should manifest itself in one way or another. The most direct way of detecting such a variation would be through observation of the neutrino spectrum. The authors have performed such a comparison [22], and have show that for certain values of the oscillation parameters, the ν_e -flux can be suppressed in radically different ways for each model (at a fixed counting rate).

How does the VEP analysis hold up in light of the reported results of non-solar neutrino experiments? It has been suggested [10] that a two-flavor model is insufficient to explain solar, atmospheric, and reactor neutrino data all at once (unless the potential of the supercluster dominates [23]); furthermore a degenerate-mass VEP mechanism could be ruled out by an

improvement of the recent LSND experiments [10].

Other possible realizations of the VEP mechanism await more detailed study. For example, the effects of ν_e -regeneration as the solar neutrinos pass through the Earth can provide yet another test for both the VEP and MSW mechanisms. Presently the detected asymmetry between day (D) and night (N) rates is $\frac{N-D}{N+D} = 0.07 \pm 0.08$ [24] and so such observations need a considerable amount of refinement before such a test would be viable. Another viewpoint on the VEP mechanism was recently expressed in ref. [23], in which the dominant potential that induces flavor oscillation was assumed to be that of the Great Attractor (or local supercluster), which is constant, and larger than the maximum solar potential by almost an order of magnitude (10^{-5}). A similar recent study of high energy neutrinos from distant AGN [25] supposes that this potential will be the one neutrinos couple to as they propagate through the intergalactic medium. An investigation of the effects of various potentials (constant and varying) on VEP oscillations is currently under way [26].

Clearly, the notion of testing the Equivalence Principle via neutrino flavor conversions is still an active and exciting field, promising many new and interesting results. With the advent of such detectors as Superkamiokande [27] and SNO [28], able to measure at the least the *entire* (flavor-independent) solar neutrino spectrum, the SNP may be on its way to becoming the SNE, or Solar Neutrino Effect.

Acknowledgements

This work was supported in part by the Natural Sciences and Engineering Research Council of Canada.

References

- [1] R. Davis, D. S. Harmer, and K. C. Hoffman, Phys. Rev. Lett. **20**, 1205 (1968); SAGE Collaboration, J. N. Abdurashidov *et al.*, Phys. Lett. **B328**, 234 (1994); GALLEX Collaboration, P. Anselmann *et al.*, Phys. Lett. **B327**, 377 (1994); Kamiokande II Collaboration, K. Hirata *et al.*, Phys. Rev. Lett. **65**, 1297 (1990)

- [2] J. N. Bahcall, *Neutrino Astrophysics*, Cambridge University Press, 1988.
- [3] S. P. Mikheyev and A. Yu. Smirnov, *Yad. Fiz.* **42**, 1441 (1985); *Phys. Lett.* **B21**, 560 (1988).
- [4] L. Wolfenstein, *Phys. Rev.* **D17**, 2369 (1978).
- [5] Stephen J. Parke, *Phys. Rev. Lett.* **57**, 1275 (1986).
- [6] M. Gasperini, *Phys. Rev.* **D38**, 2635 (1988).
- [7] *Phys. Rev.* D52 (1995) 1770-1779..
- [8] J. Pantaleone, A. Halprin, and C. N. Leung, *Phys. Rev.* **D47**, R4199 (1993).
- [9] M. N. Butler *et al.*, *Phys. Rev.* **D47**, 2615 (1993).
- [10] R.B. Mann and U. Sarkar, *Phys. Rev. Lett.* **76** 865 (1996).
- [11] C. Athanassopoulos *et. al.*, *Phys. Rev. Lett.* **75** (1995) 2650; B.T. Cleveland *et. al.* *Nucl. Phys.* **B38** (Proc. Supp.) (1995) 47.
- [12] H. Minakata and H. Nunokawa, KEK-TH-396/TMUP-HEL-9402, (hep-ph 9405239) (April 1994); also *Phys. Rev.* **D51**, 6625 (1995).
- [13] See, for example M. J. Longo, *Phys. Rev. Lett.* **60**, 173 (1988); L. M. Krauss and S. Tremaine, *Phys. Rev. Lett.* **60**, 176 (1988).
- [14] C. W. Misner, K. S. Thorne, and J. A. Wheeler, *Gravitation*, W. H. Freeman and Co. San Francisco (1973).
- [15] V. Barger *et al.*, *Phys. Rev.* **D22**, 2718 (1980).
- [16] H. W. Zaglauer and K. H. Schwarzer, *Phys. Lett.* **B198** 556 (1987).
- [17] A. Baldini and G. F. Giudice, *Phys. Lett.* **B186**, 211 (1987).

- [18] J. N. Bahcall and M. H. Pinsonneault, *Rev. Mod. Phys.* **64**, 885 (1992).
- [19] Hisakazu Minakata, hep-ph/9504222 (1995); also *Phys. Lett.* **B356** 61–67, (1995).
- [20] N. Hata and P. Langacker, *Phys. Rev.* **D50**, 632 (1994).
- [21] X. Shi and David N. Schramm, FERMILAB-Pub-91/178-A (1991).
- [22] J. Mureika and R. B. Mann, *Phys. Lett.* **B368** 112 (1996).
- [23] A. Halprin, C. N. Leung, and J. Pantaleone, hep-ph/9512220.
- [24] Kamiokande Collaboration, *Proceedings of the 16th International Conference on Neutrino Physics and Astrophysics* (1994; to appear).
- [25] H. Minakata and A. Yu. Smirnov, hep-ph/9601311.
- [26] J. Mureika and R. B. Mann, *Work in progress*.
- [27] Y. Totsuka, “Superkamiokande”, Univ. of Tokyo Report No. ICRR-227-90-20, 1990
- [28] G.T. Ewan et.al., “Sudbury Neutrino Observatory Proposal” *Trends in Astroparticle Physics*, (Santa Monica 1990 Proceedings) 571.

Expt.	R_{ν_e}	ΔR	Units
Homestake	2.55	0.25	SNU
SAGE	73	19.3	SNU
GALLEX	79	11.7	SNU
KII	0.51	0.07	Φ_{8B}^{SSM}

Table 1: Recent reported rates from various solar neutrino detector experiments. Errors (ΔR) are quoted to 1σ -uncertainty.

\mathcal{M}	$R_{\nu_e}^{SSM}$				Total
	8B	7Be	pp	Other	
${}^{37}Cl$	6.1	1.1	0.0	0.9	8.0 ± 1.0 SNU
${}^{71}Ga$	14.0	34.3	70.8	11.9	132^{+20}_{-17} SNU
ν_e-e	5.8	0.0	0.0	0.0	$5.8 \pm 2.1 \times 10^6 \text{cm}^{-2}\text{s}^{-1}$

Table 2: Theoretical counting rates for material- \mathcal{M} -based detectors.

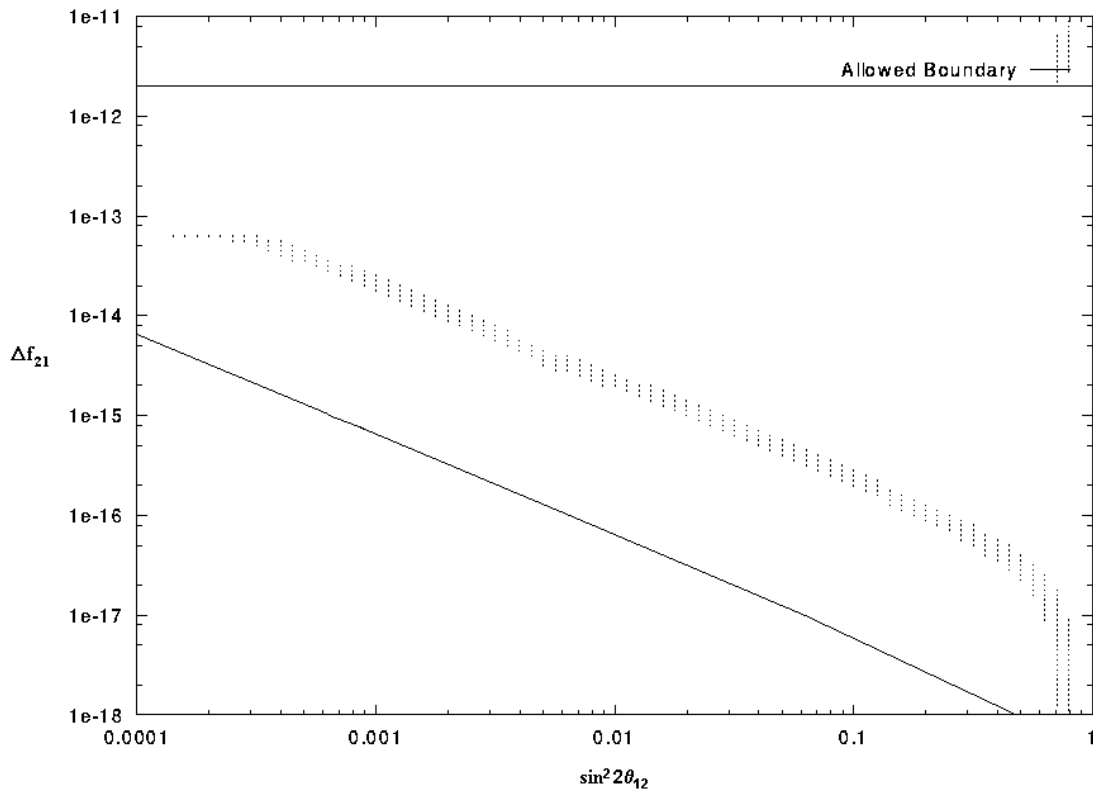


Figure 1: 2-flavor limit, 2σ range.

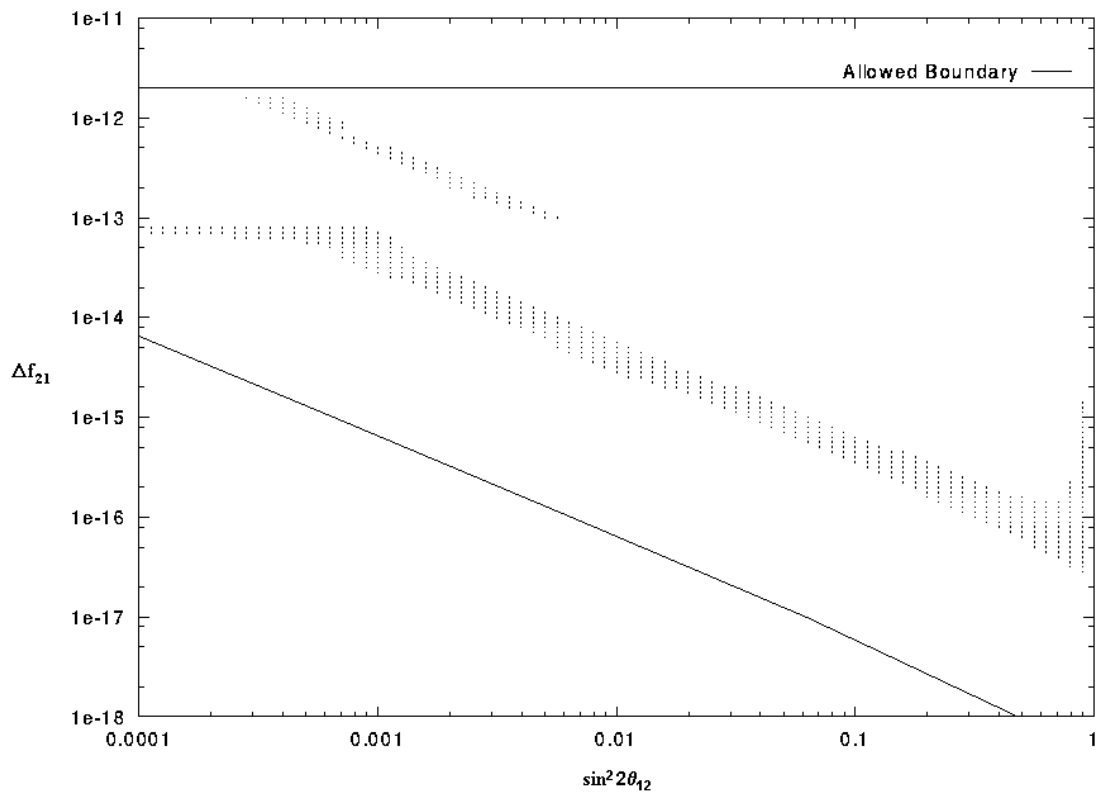


Figure 2: 2-flavor limit, 3σ range.

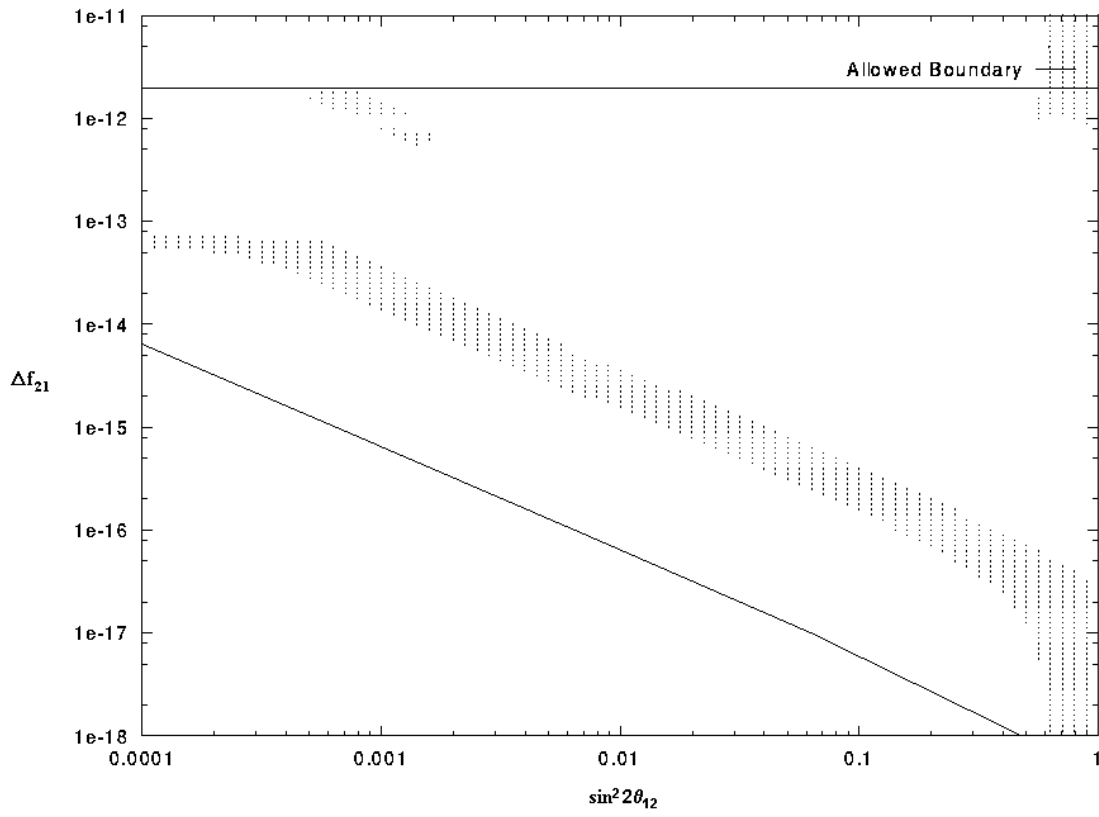


Figure 3: Lower flux limit, 2-flavors, 3σ range.

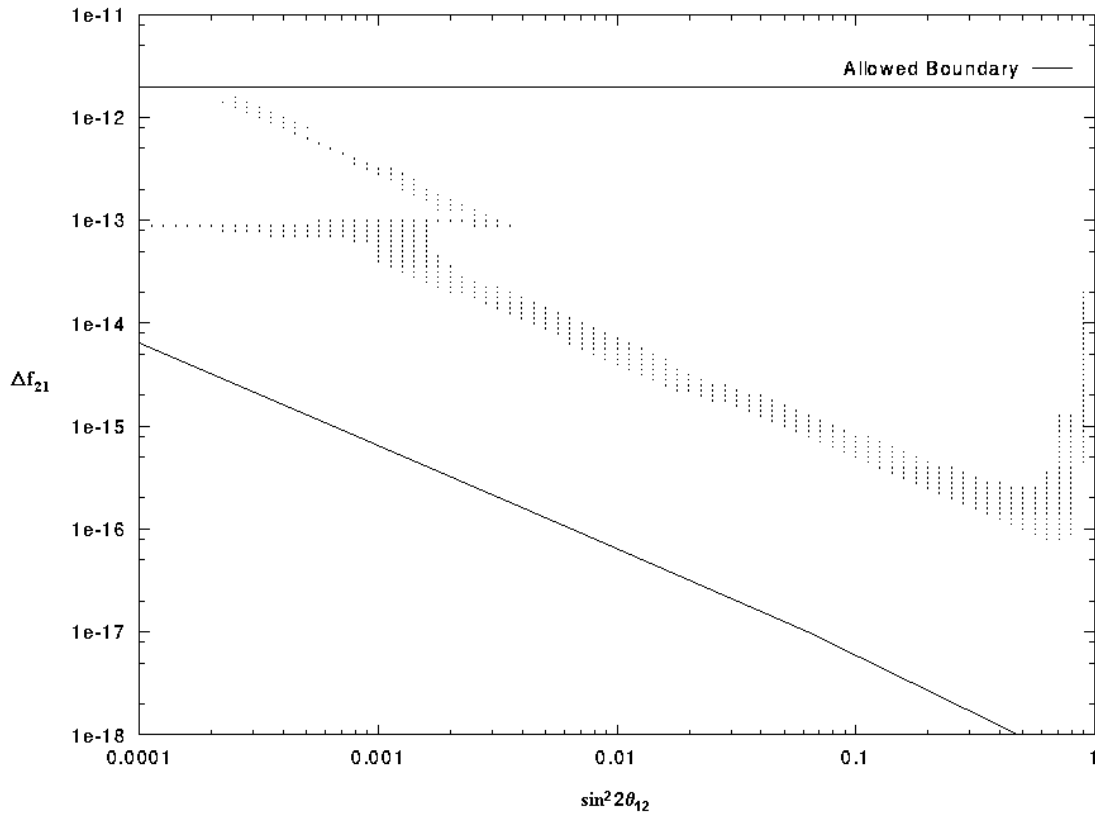


Figure 4: Upper flux limit, 2-flavors, 3σ range.

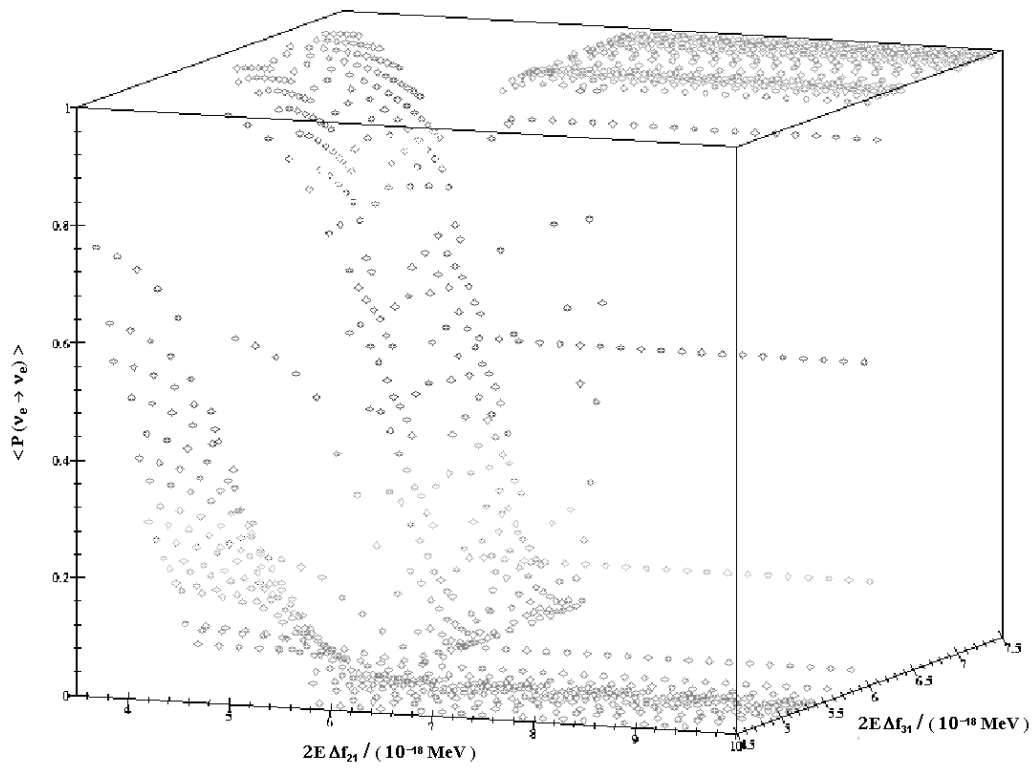


Figure 5: $\sin^2 2\theta_{12} = 5 \times 10^{-3}$; $\sin^2 \theta_{13} = 10^{-3}$

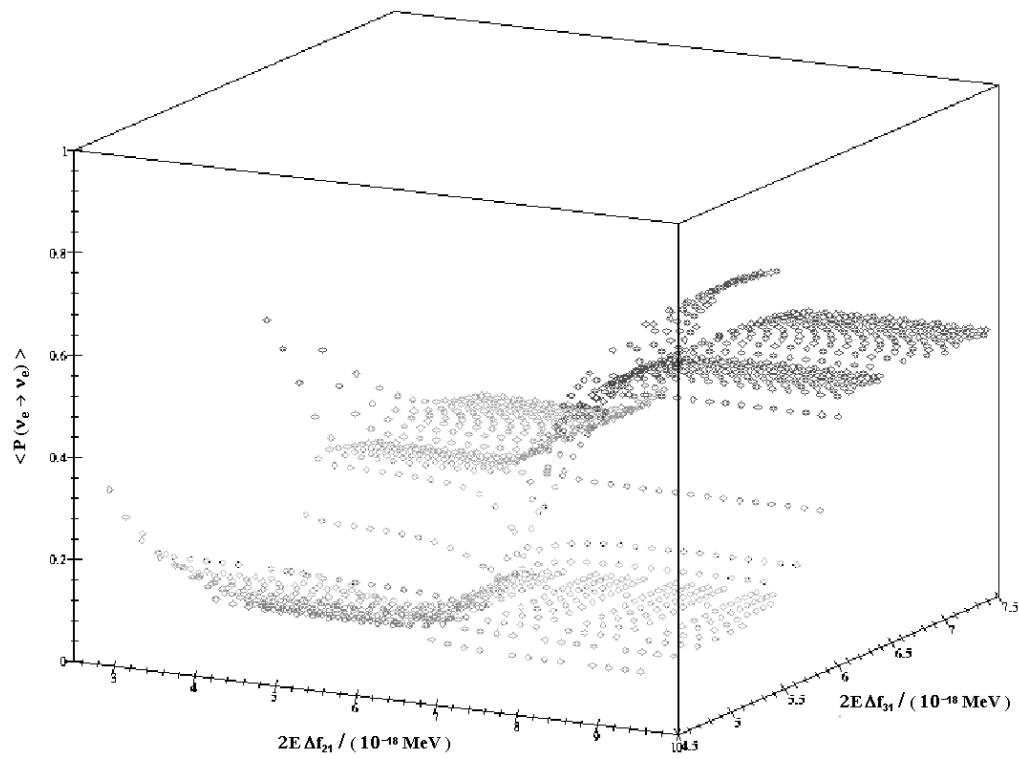


Figure 6: $\sin^2 2\theta_{12} = 0.8$; $\sin^2 \theta_{13} = 10^{-3}$

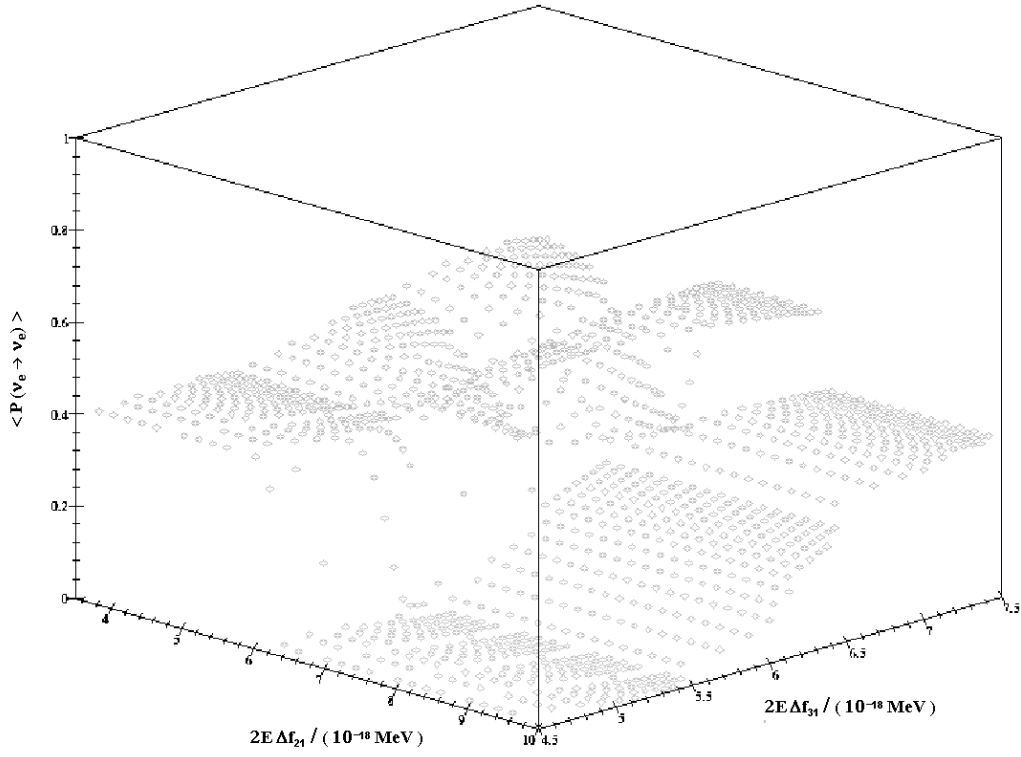


Figure 7: $\sin^2 2\theta_{12} = 5 \times 10^{-3}$; $\sin^2 \theta_{13} = 0.4$

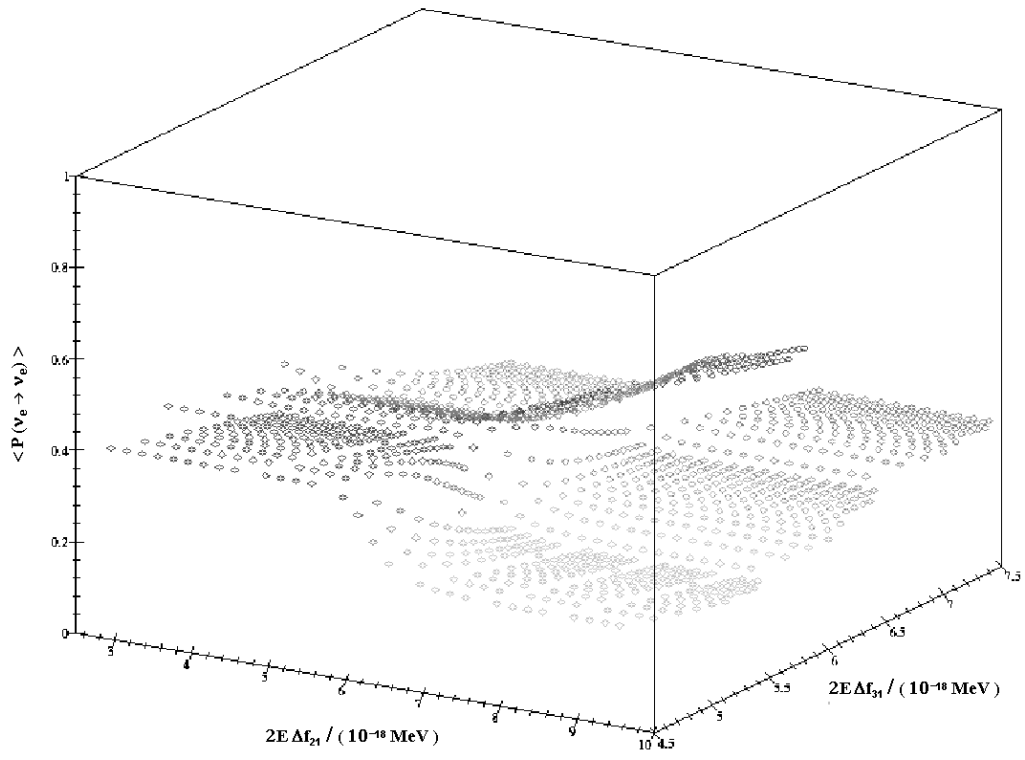


Figure 8: $\sin^2 2\theta_{12} = 0.8; \sin^2 \theta_{13} = 0.4$

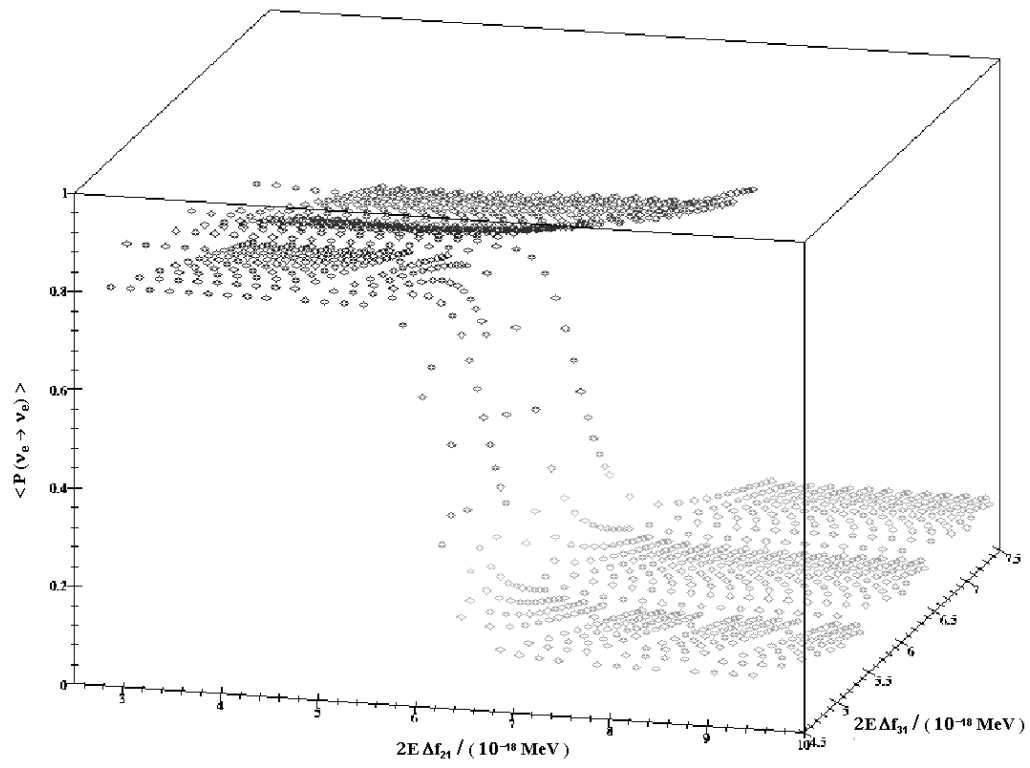


Figure 9: $\sin^2 2\theta_{12} = 0.8$; $\sin^2 \theta_{13} = 0.8$

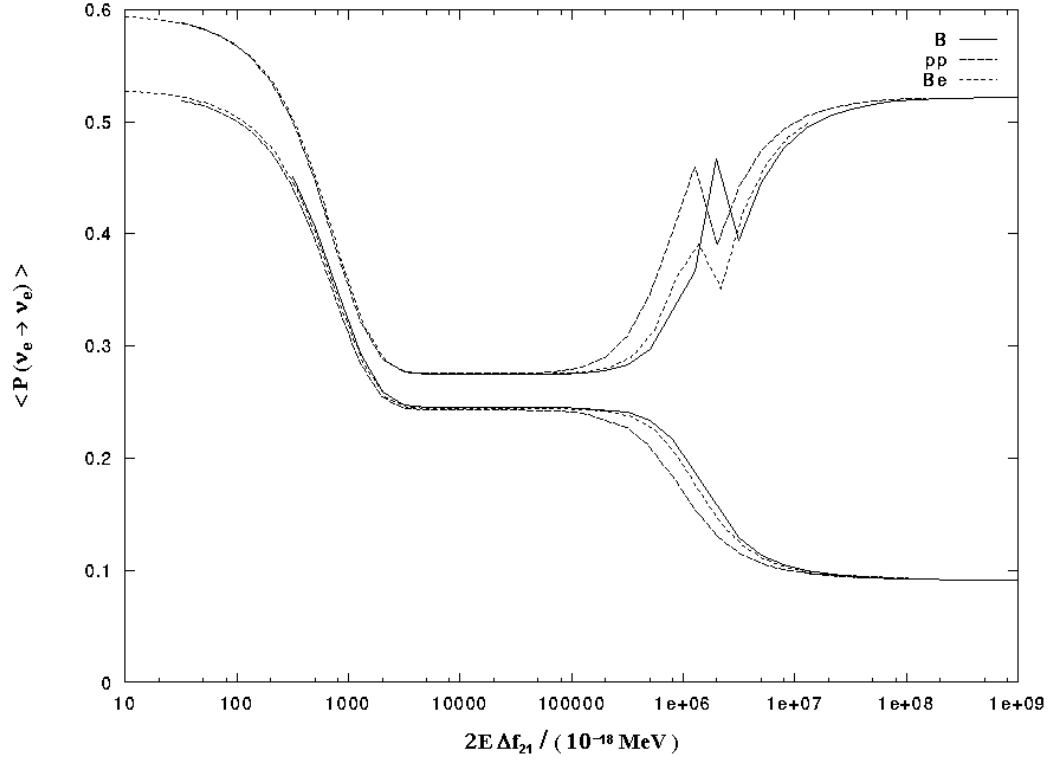


Figure 10: $\langle P(\nu_e \rightarrow \nu_e) \rangle$ for ${}^8\text{B}$, ${}^7\text{Be}$, and pp neutrinos, fixed values of $2E\Delta f_{31}/(10^{-18} \text{ MeV}) = 2 \times 10^4$ (lower), and 2×10^6 (upper). $s_{2\theta_{12}} = 0.8$; $s_{13}^2 = 10^{-3}$

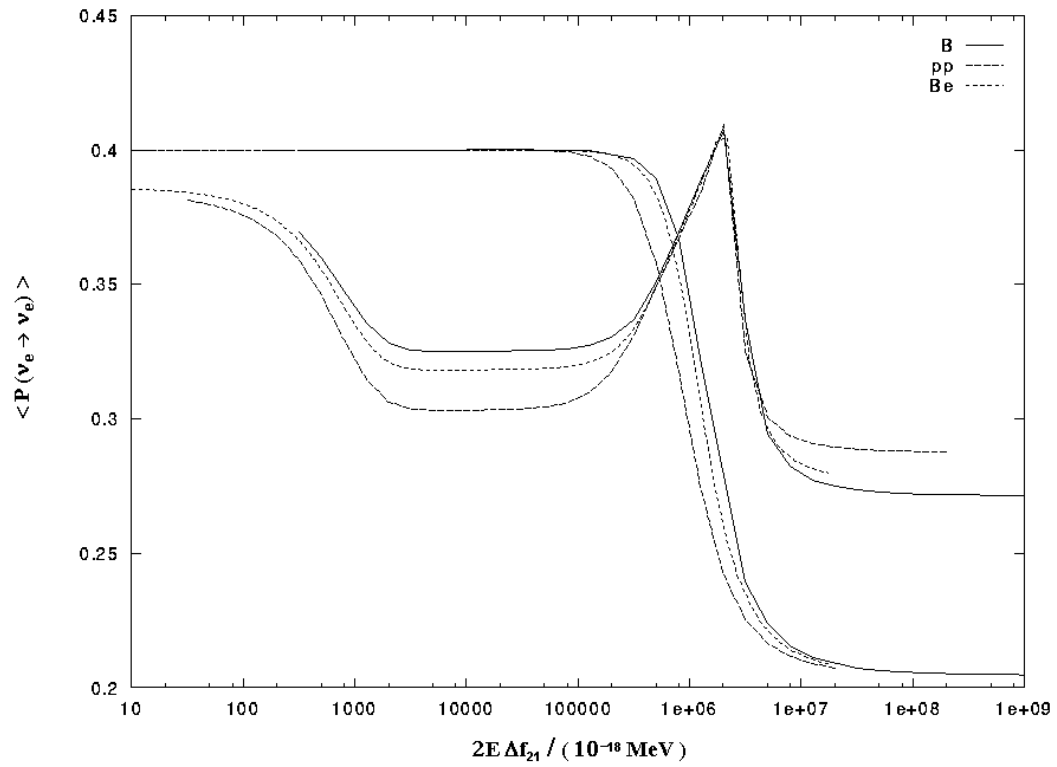


Figure 11: $\langle P(\nu_e \rightarrow \nu_e) \rangle$ for ${}^8\text{B}$ and pp neutrinos, same values of $2E\Delta f_{31}$ (“tub”-shaped curve is 2×10^6). $s_{2\theta_{12}} = 0.8$; $s_{13}^2 = 0.4$

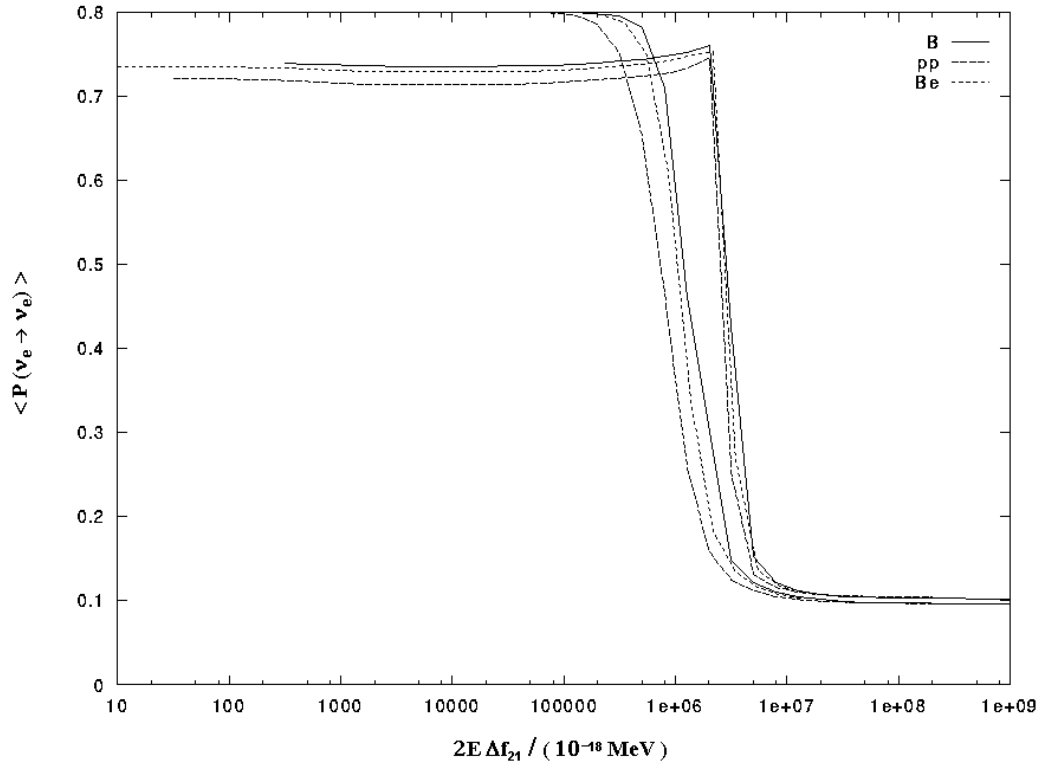


Figure 12: $\langle P(\nu_e \rightarrow \nu_e) \rangle$ for 8B , 7Be and pp neutrinos, $2E\Delta f_{31} = 2 \times 10^4$ (left) and 2×10^6 (right). $s_{2\theta_{12}}^2 = 0.8$; $s_{13}^2 = 0.8$.

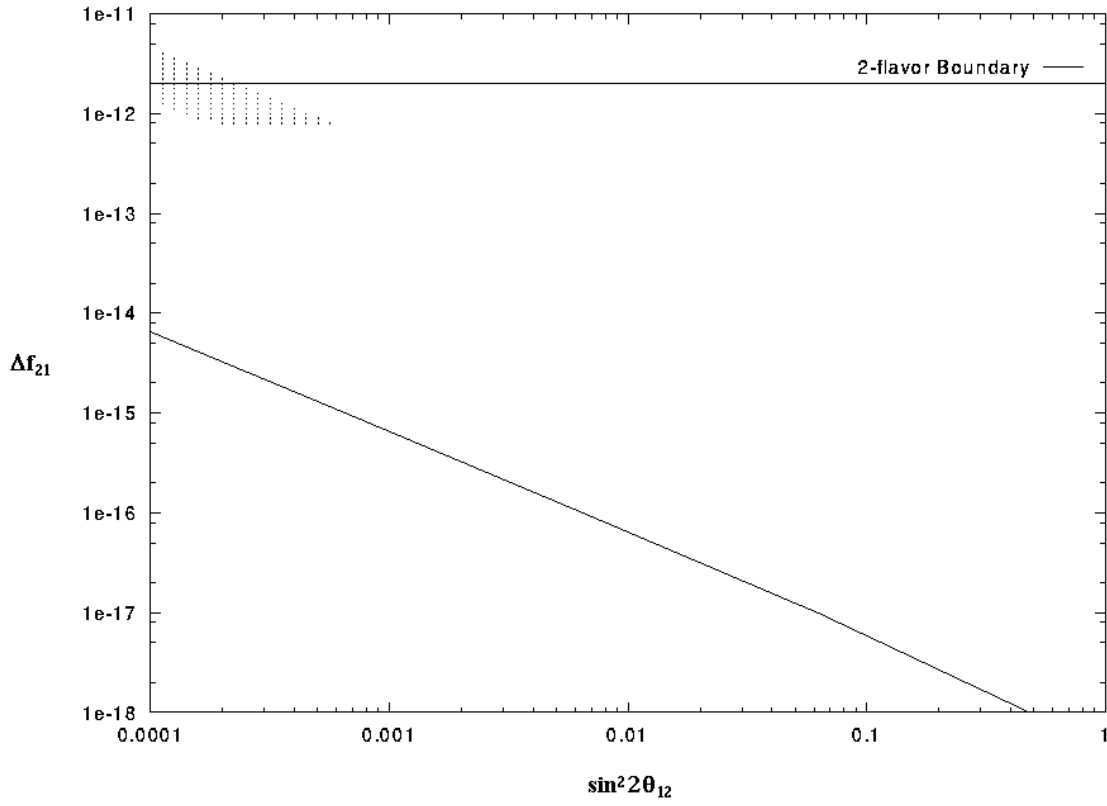


Figure 13: $\Delta f_{31} = 10^{-13}$; $s_{13}^2 = 10^{-3}$, 3σ C.L.

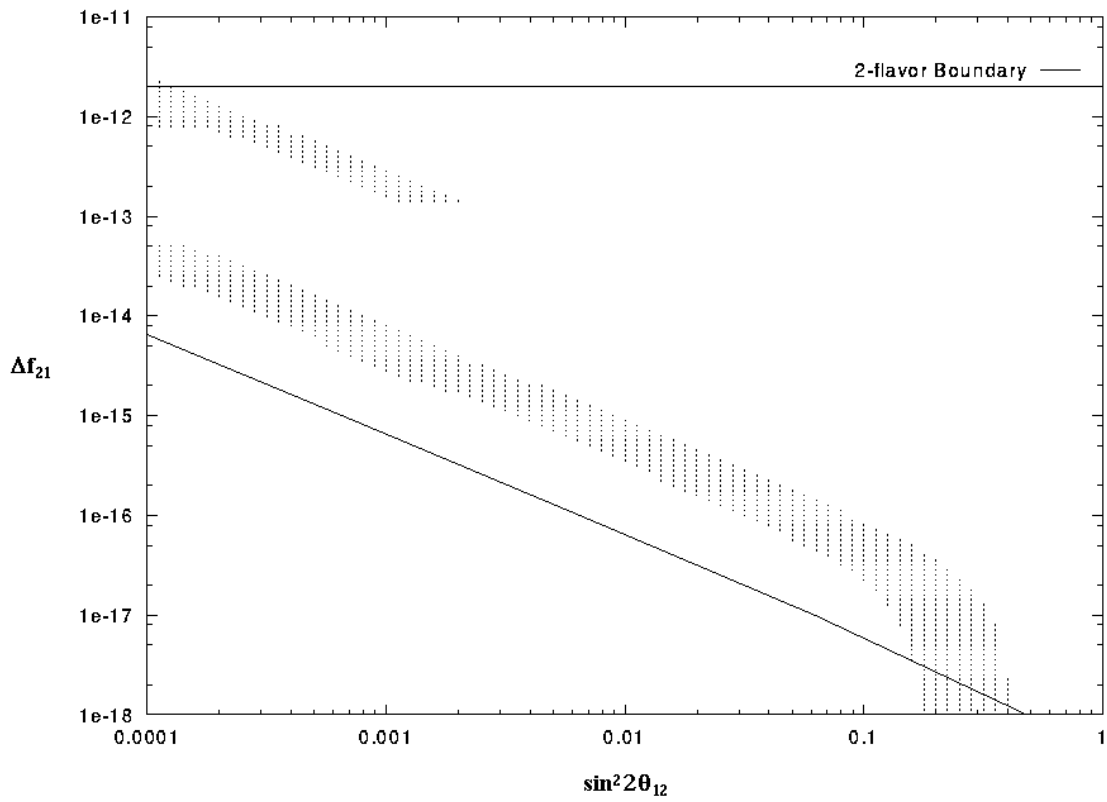


Figure 14: Upper flux limit, $\Delta f_{31} = 10^{-13}$; $s_{13}^2 = 10^{-3}$, 3σ C.L.

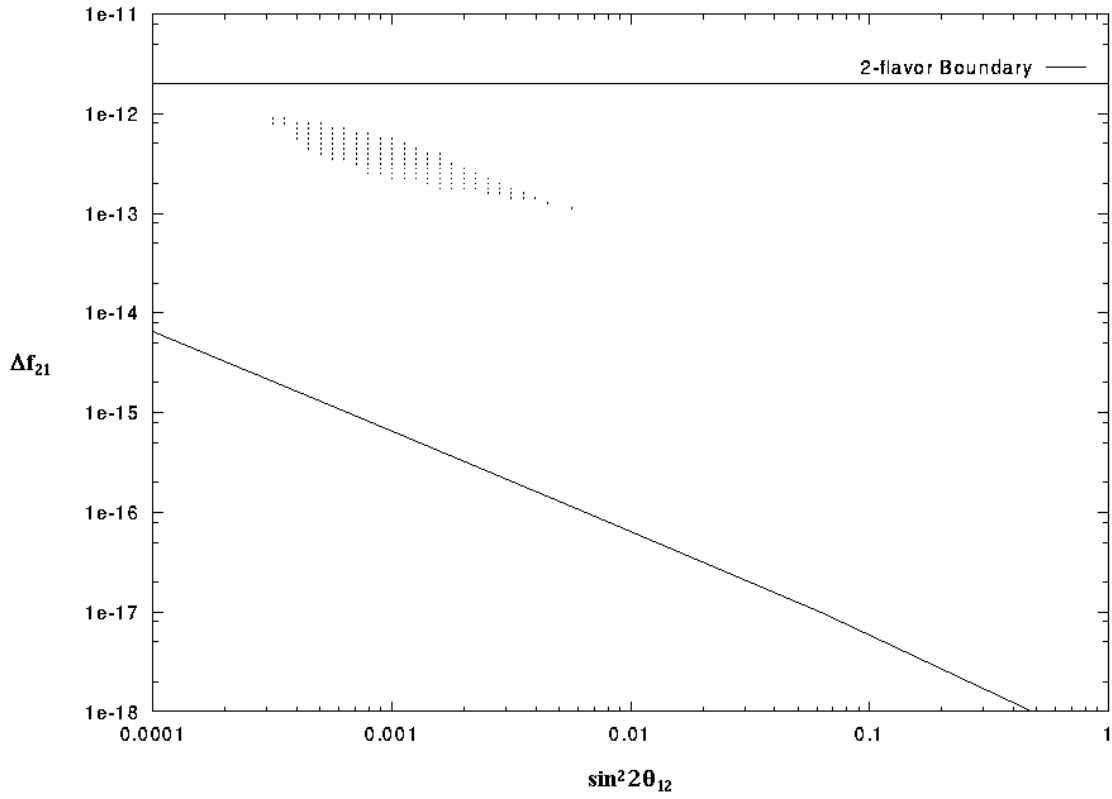


Figure 15: $\Delta f_{31} = 10^{-13}$; $s_{13}^2 = 10^{-4}$, 3σ C.L.

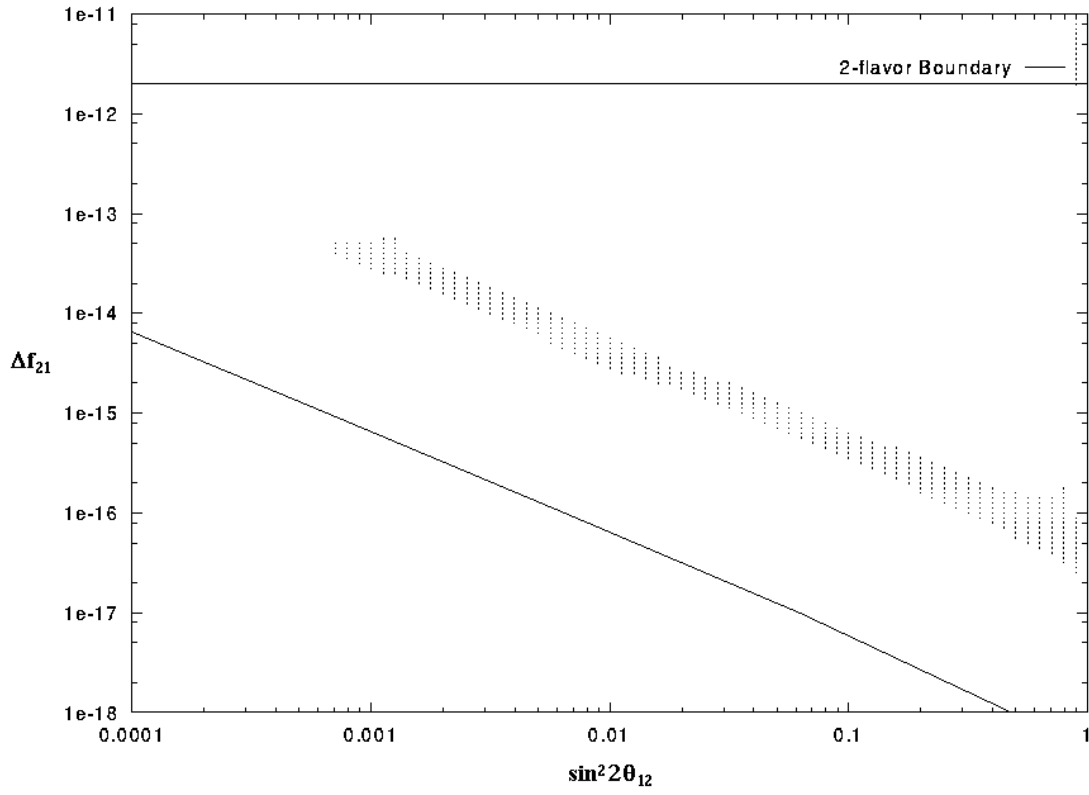


Figure 16: $\Delta f_{31} = 10^{-12}$; $s_{13}^2 = 10^{-4}$, 3σ C.L.

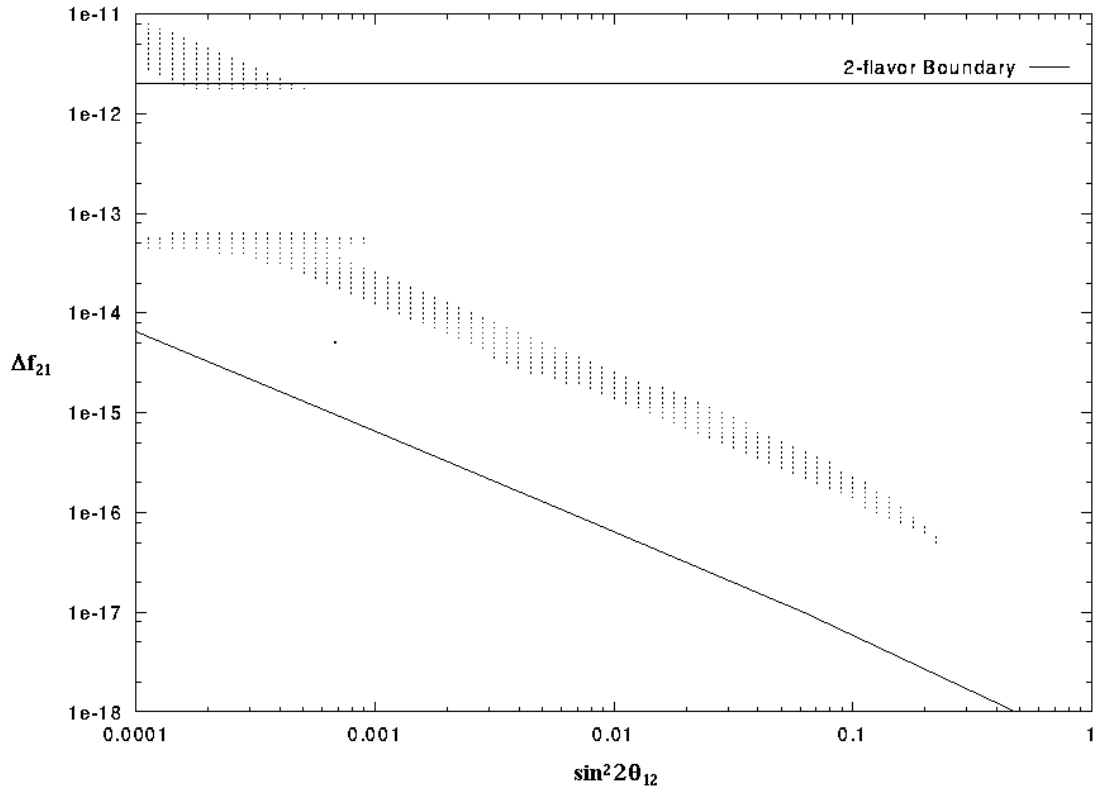


Figure 17: $\Delta f_{31} = 10^{-12}$; $s_{13}^2 = 0.2$, 3σ C.L.

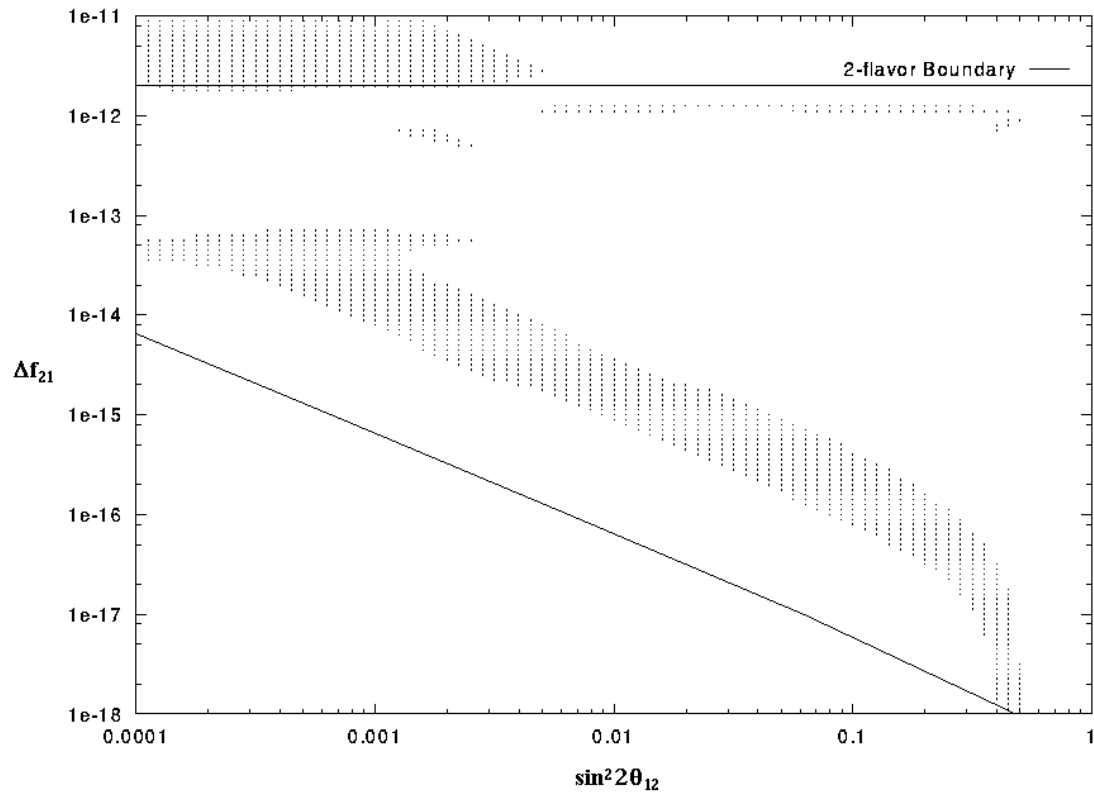


Figure 18: $\Delta f_{31} = 10^{-12}$; $s_{13}^2 = 0.3$, 3σ C.L.

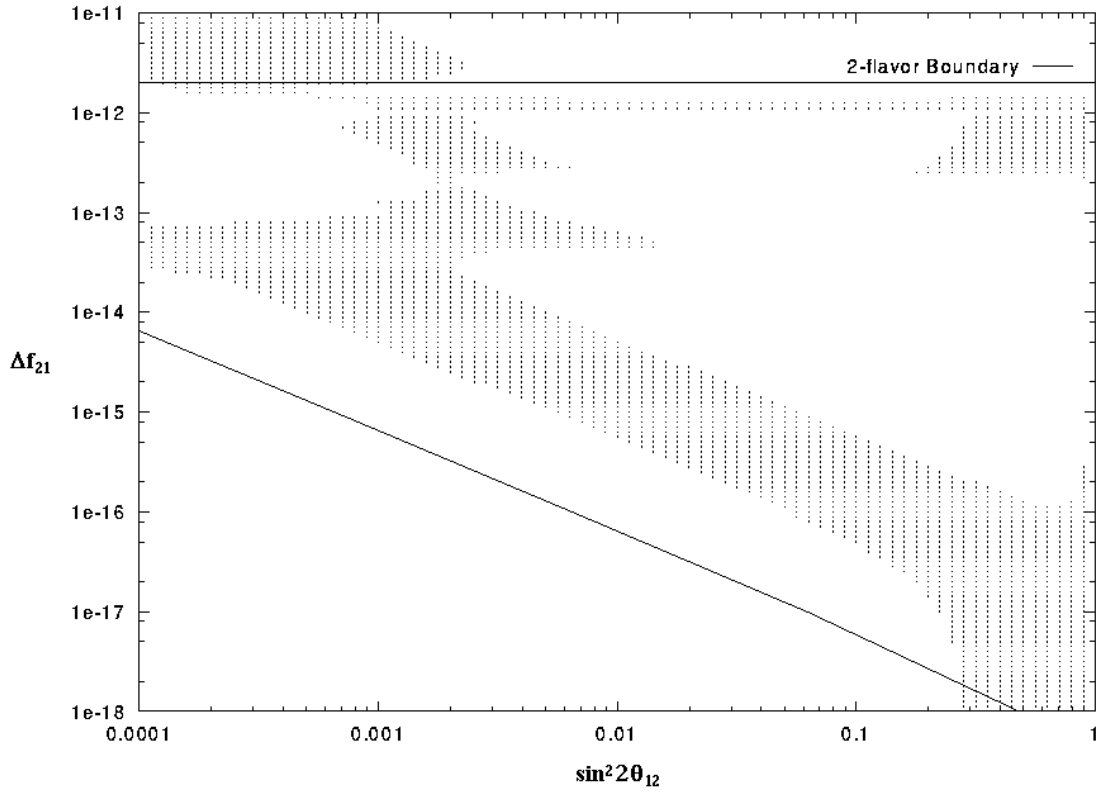


Figure 19: $\Delta f_{31} = 10^{-12}$; $s_{13}^2 = 0.4$, 3σ C.L.

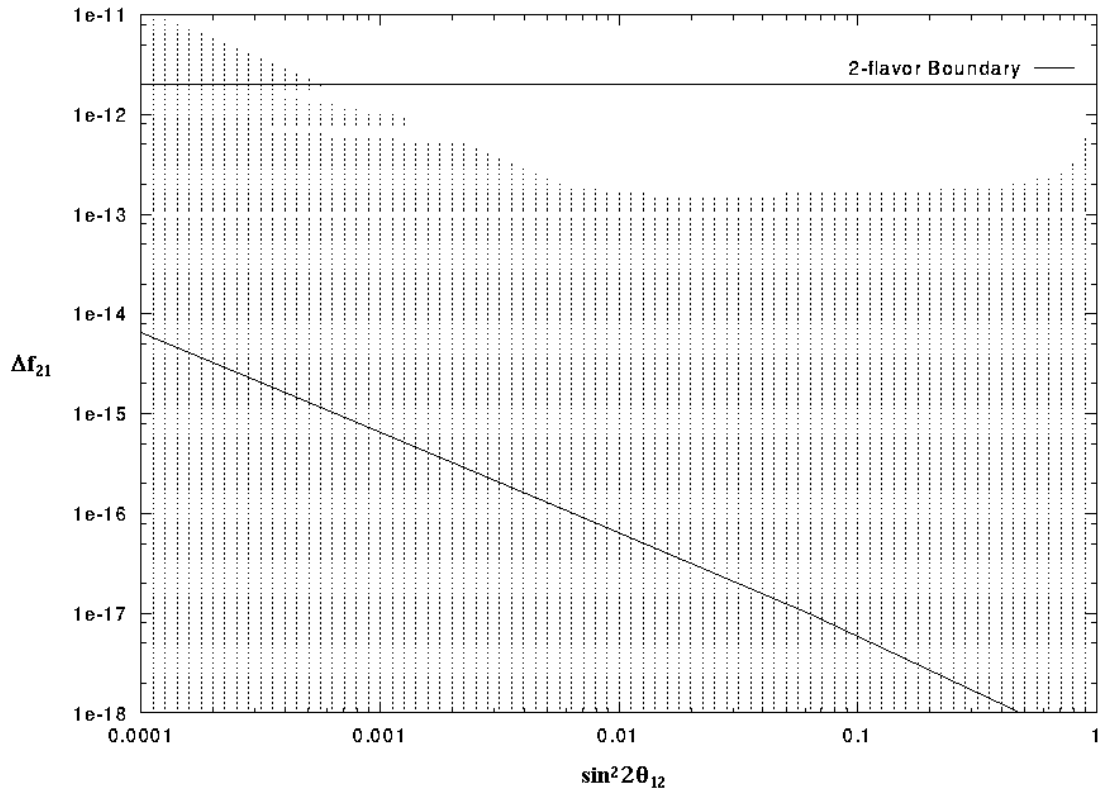


Figure 20: $\Delta f_{31} = 10^{-13}$; $s_{13}^2 = 0.4$, 3σ C.L.

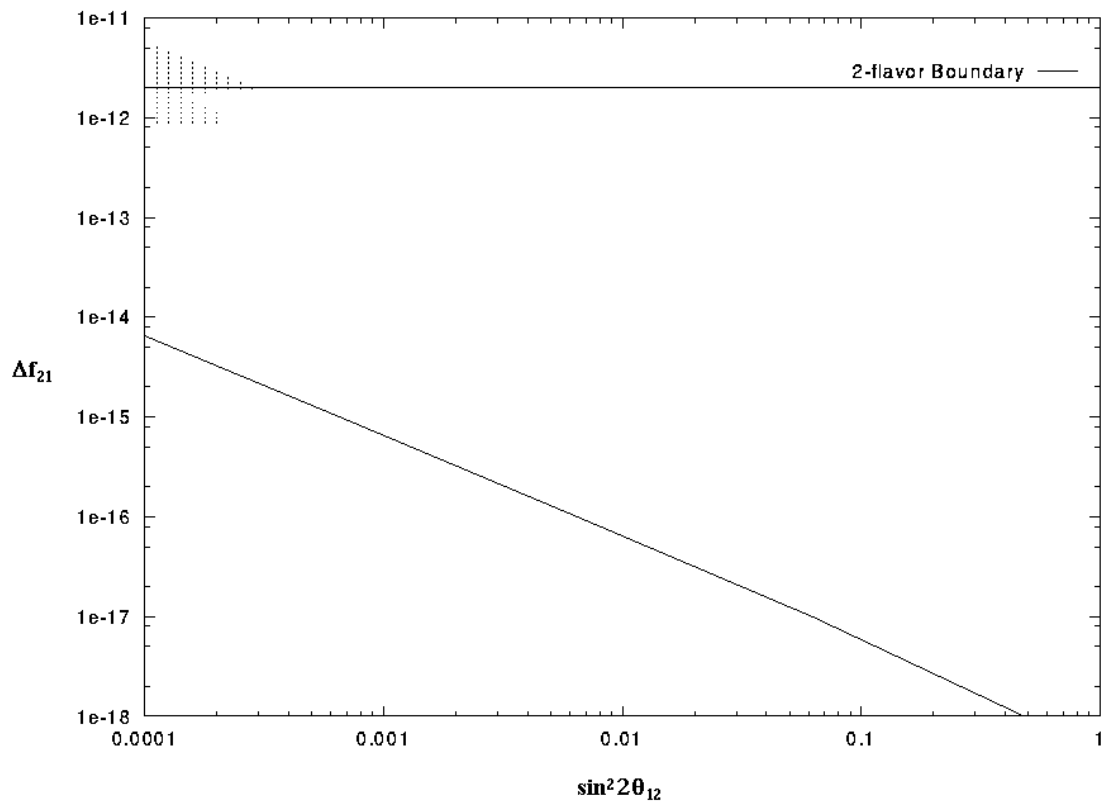


Figure 21: $\Delta f_{31} = 10^{-13}$; $s_{13}^2 = 0.4$, 2σ C.L.

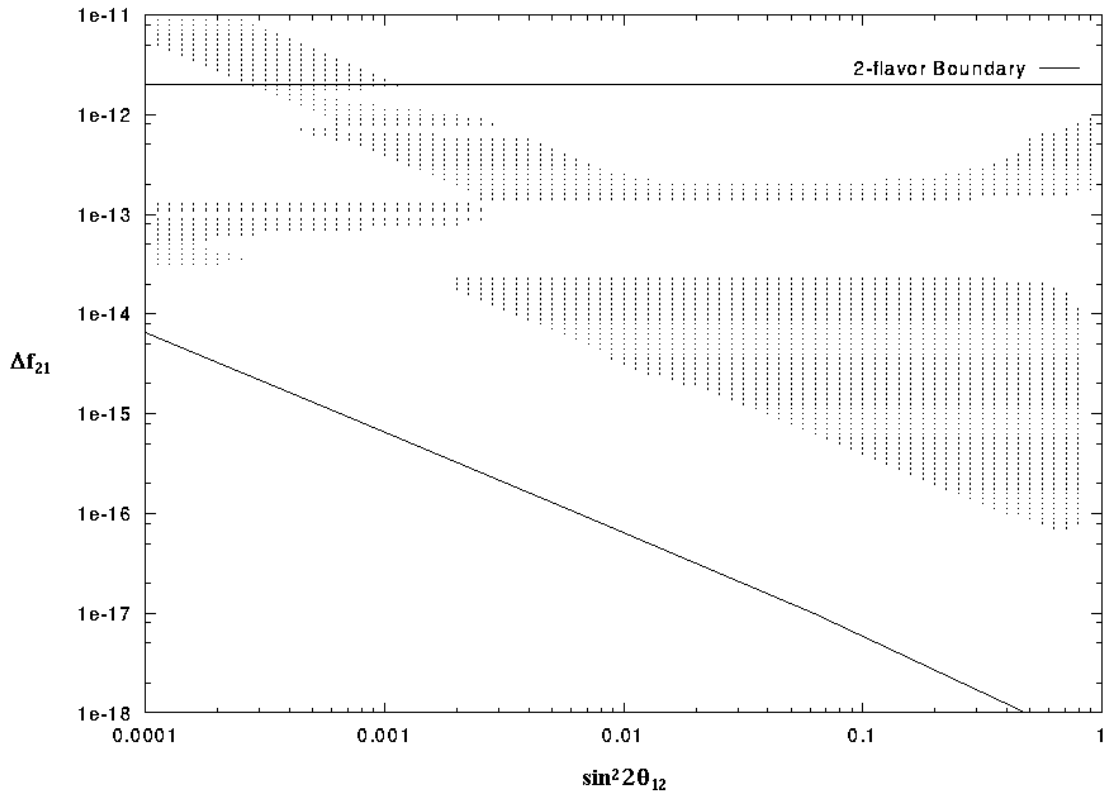


Figure 22: Upper flux limit, $\Delta f_{31} = 10^{-13}$; $s_{13}^2 = 0.4$, 3σ C.L.